The Effect of Galvanized Steel Corrosion on the Integrity of Concrete

by

Zuo Quan Tan

A thesis
presented to the University of Waterloo
in fulfillment of the
thesis requirement for the degree of
Master of Applied Science
in
Civil Engineering

Waterloo, Ontario, Canada, 2007

Author's Declaration

I hereby declare that I am the sole author of this thesis. This is a true copy of the thesis, including any required final revisions, as accepted by my examiners.

I understand that my thesis may be made electronically available to the public.

Signature

Abstract

The major concern regarding the use of hot-dip galvanized (HDG) steel as reinforcement in concrete has been the high rate of corrosion experienced by the zinc during the first hours in the fresh, wet, and highly alkaline concrete. The present work was aimed at clarifying three issues associated with these concerns. The first involves the metallurgical phases at the surface of the zinc coating. The concentration of zinc at the surface is a function of processing procedures, surface treatment, and exposure to weathering. Differences in the coating surface composition influence the corrosion behaviour of HDG steel reinforcing bars when they are embedded in concrete. The second issue involves the increasing use of supplementary cementing materials in concrete, which change the chemistry of the concrete pore fluid, and also influence the corrosion. The third issue is that the initial corrosion is accompanied by hydrogen evolution, which could increase the pore volume of adjacent cement and thereby, decrease the bond stress between the concrete and the steel. In order to limit the hydrogen evolution, a chromate layer is applied after galvanizing.

The results of the project have demonstrated that, during zinc corrosion in ordinary Portland cement (OPC) concrete, calcium hydroxyzincate formed on untreated HDG steel provided sufficient protection against corrosion. Therefore, it is concluded that treating HDG rebar with dilute chromic acid is unnecessary as a method of passivating zinc. A layer of zinc oxide and zinc carbonate formed through weathering on HDG bars slightly increased the initial corrosion rate and passivation time compared with the non-weathered rebars. HDG steel with an alloyed coating, i.e. consisting of Fe-Zn intermetallic phases, required a longer time to passivate than those with a pure zinc surface layer. The lower zinc content of the surface limited the rate of CHZ formation and, hence, delayed passivation. However, regardless of the surface condition, the coating depth loss after two days of embedment in OPC concrete was insignificant.

In concretes containing 8% cement replacement with silica fume, or 25% cement replacement with slag, the initial corrosion rates were higher than those in OPC due to higher pH and lower calcium contents of the concrete pore solution. The higher corrosion rates lead to initial depth losses which are considered significant. However, in these concretes, chromate treatment was also shown to be unnecessary.

Through porosity assessment of cements adjacent to HDG bars, it was found that hydrogen evolution accompanying zinc corrosion did not have an impact on the pore volume of cements: any

additional pores created by hydrogen gas are filled by the zinc corrosion products. The negligible difference in pore volume between cements adjacent to chromated and non-chromated bars further confirmed that chromated treatment was unnecessary.

.

Acknowledgements

I would like to express the deepest appreciation to my supervisor, Professor Carolyn Hansson, for her invaluable guidance and support throughout the course of this research project and in completing this dissertation. She has consistently conveyed a spirit of adventure in regard to research and scholarship and more importantly she has supplied a model for living and contributing to society that I will follow throughout my life and career.

This project would not have been possible without the help of my colleagues and friends; Dr. Laura Mammoliti, Dr. Amir Poursaee, Dr. Shahzma Jaffer, Ramtin Movassaghi, Khanh Tran, Irene Wijoyo, Kyle Anders, Brad Bergsma, Ken Su, and Katherine Olsen. I would like to give special thanks to Dr. Amir Poursaee for his tremendous assistance with operating the electrical equipment used in this project and for his Automatic Corrosion Monitoring Program, without which the corrosion experiments would not have been possible.

I would like give thanks to Randy Fagan from the Department of Physics for his assistance with Raman spectroscopy and pore solution extraction. I also appreciate the efforts of Civil Engineering Technicians Richard Morrison and Douglas Hirst for their assistance in concrete casting.

Thanks to the International Lead and Zinc Research Organization (ILZRO) and City of Calgary for providing their financial support, and Pure Metal Galvanizing, Galvcast Manufacturing Inc., Essroc Italcementi Group, and Teck Cominco Ltd. for providing materials and technical assistance. I am extremely grateful for the advice and guidance of Doug Rourke from ILZRO regarding various aspects of the project.

I would like to thank my parents, sister, and numerous friends who endured this long process with me, giving me strength when I needed it. Lastly, I truly appreciate the invaluable help from my friend Tyson in editing this dissertation.

Dedication

This work is dedicated:

to my parents and sister;

and

to Carolyn Hansson

Table of Contents

List of Figures

List of Tables

Chapter 1
Introduction

Corrosion of steel is a major cause of reinforced concrete structure degradation, and in extreme cases, failure. To protect the steel from corrosion, a zinc coating is applied through the process of hot dip galvanizing (HDG). The zinc coating protects the steel in two ways: one by acting as a physical barrier and the other by cathodic protection in the event of local breakdown of the coating that exposes the bare steel. Corrosion of the bare steel, therefore, does not commence until a large area of the zinc coating completely dissolves. The zinc coating is known to be stable in concrete without chloride contamination or carbonation. Furthermore, it has a four to five times higher tolerance to chloride induced corrosion. Despite the improved long term corrosion resistance of HDG steel compared to that of bare steel, there are uncertainties concerning its initial corrosion when embedded in concrete. In fresh concrete, the zinc coating is thermodynamically unstable and corrodes vigorously within the first few days due to the high pH of the pore solution. This process continues until passivation occurs as a result of formation of a protective zinc corrosion product layer. Since the extent of protection provided by the zinc coating is a function of its thickness, ascertaining the depth of zinc loss during this initial corrosion is crucial.

Evaluating the impact of hydrogen evolution, which accompanies the corrosion, on the integrity of concrete is also important. Currently, there are conflicting views regarding the consequences of hydrogen evolution in the literature. One view postulates that hydrogen gas increases the porosity of cement adjacent to the steel, thereby weakening the bond between the concrete and the reinforcing bar [1]. The other postulates that the long term effect is negligible because the pores produced by hydrogen in the fresh cement paste are filled with the corrosion products of zinc [2-4]. Literature regarding this issue has yet been inconclusive which elicits the need for further research in the present work.

A third factor in this study involves the need for chromating the HDG rebars. To date, in North America, a hexavalent chromate film is applied to the zinc surface, minimizing zinc corrosion, thereby, reducing the amount of hydrogen gas evolved. However, due to the health hazards associated with the handling of hexavalent chromate solutions, it is being banned in Europe and similar restrictions are under consideration in North America; therefore, it is important to determine the impact of eliminating the chromates on the corrosion performance of the galvanized rebar.

The corrosion behaviour of the zinc coating in alkaline solution is highly dependent on pH such that passivation is only possible at pH less than 13.3±0.1. At higher pH levels, the corrosion products are not protective and corrosion continues [5], rapidly consuming the coating. In today's high performance concretes, supplementary cement materials such as slag and silica fume are commonly used, which upon hydration react with alkalis, lowering the pH and thus influencing the corrosion behaviour of the zinc. It was anticipated that the lower pH might prove beneficial and, so, this aspect of the corrosion has also been studied.

Furthermore, corrosion is affected by variation in the coating surface composition when embedded in concrete. Due to variation in galvanizing procedures, composition of the bare steel, and storage methods, the metallurgical nature and surface composition of the zinc coating can differ. For example, steel with a high silicon content is highly reactive with molten zinc, quickly forming a coating that comprises entirely of iron-zinc alloy phases. Similarly, if the quenching rate is too slow, sufficient intermetallic diffusion will occur, also leading to a fully alloyed coating. Less reactive steel in conjunction with a faster quench rate typically results in a coating with alloyed phases adjacent to the steel and a surface layer of pure (>95%) zinc. Prior to embedment in concrete, galvanized rebars are typically stored outdoors and undergo weathering for an extended period of time, leading to the formation of zinc oxide and zinc carbonate on the surface. These processes may potentially affect the corrosive behaviour of the coating.

Based on this discussion, the objectives of this study are:

1. To determine the influence of the above surface conditions on the initial corrosion behaviour and to ascertain the depth loss and the time to passivation of the different bars.
2. To assess the influence on the corrosion behaviour due to the addition of silica fume and ground granulated blast furnace slag to concrete.
3. To quantify the porosity of the cement adjacent to the galvanized steel to evaluate the severity of hydrogen evolution.

Chapter 2
Literature Review

2.1 Metallurgy of Galvanized Reinforcing Steel

An economical method of providing corrosion protection to reinforcing steel is by applying a zinc coating through the process of hot-dip galvanizing. During this process, steel is immersed in a molten zinc bath at temperatures of approximately 450 to 490^{o}C. While immersed, metallurgical reactions occur between the iron and the molten zinc, resulting in the formation of an adherent coating that provides an excellent barrier to corrosive environments and cathodic protection when imperfections exist or in the event of local dissolution of the coating.

2.1.1 Iron-Zinc Equilibria and Kinetics

The metallurgical reactions that occur give rise to various intermetallic phases with descending Fe content from the substrate steel. These intermetallic phases include: gamma (γ) phase, gamma$_1$ (γ_1) phase, delta (δ) phase, zeta (ζ) phase and an eta (η) phase as illustrated in Figure 2-1.

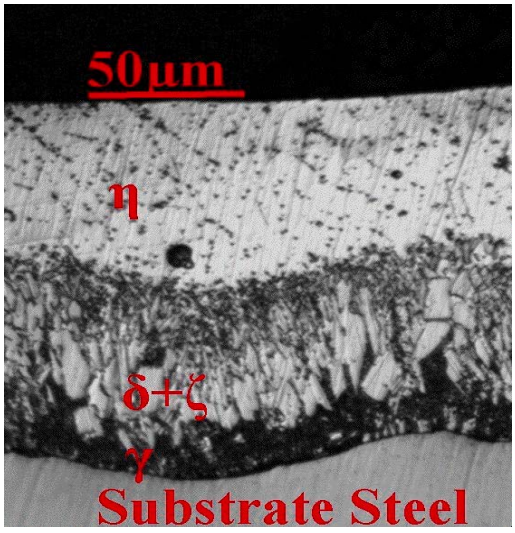

Figure 2-1. Optical micrograph showing the microstructure of the galvanized coating

The relative amount of each phase is highly dependent on the galvanization procedures and the chemistry of the substrate steel and zinc bath, which will be discussed in the succeeding section.

A detailed discussion of the Fe-Zn equilibria and kinetics can be found in the literature [6] and a brief summary is provided here. From the zinc-rich region of the binary Fe-Zn binary phase diagram, Figure 2-2, the equilibrium composition of each phase can be determined and is summarized in Table 2-1. Of the various phases, the zeta (ζ) phase (with approximately 5-6 wt% Fe) forms first, followed by the delta (δ) phase without any apparent delay. The nucleation of the gamma (γ) phases, however, occurs after some incubation time. The formation of both the zeta and delta phases take place after 5s whereas the formation of the gamma phases requires an incubation time of 30s [6]. The eta phase, though not shown in the Fe-Zn phase diagram, is a relatively pure zinc phase with approximately 0.03 wt% Fe and it is formed upon quenching.

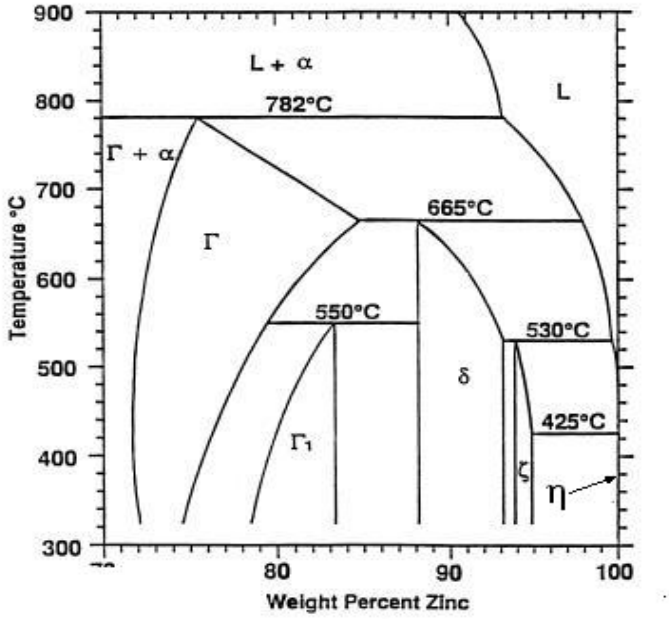

Figure 2-2. Zinc rich corner of the binary Fe-Zn phase diagram [6]

Table 2-1. Fe-Zn phase composition [6]

Phases	Formula	% Iron
αFe	Fe(Zn)	96.1
Γ	$FeZn_3$	23.5-28.0
$Γ_1$	$Fe_{20}Zn_{80}$	17.0-19.5
δ	$Fe_{10}Zn_{90}$	7.0-11.5
ζ	Fe_5Zn_{95}	5.0-6.0
η	Zn(Fe)	0.03

The growth kinetics of the coating is dependent on both the immersion time and the individual growth kinetics of the different phases. In hot-dip galvanizing, the time of immersion is short (typically up to five minutes), in which case growth of the various phases is diffusion controlled. Amongst the intermetallic phases, zeta, with the lowest iron content is, therefore, the first to nucleate at the interface of the zinc solution and the substrate steel. Zeta exhibits an rapid initial growth that decreases over time, while the delta phase exhibits a slow initial growth that increase with time [6]. The gamma phases as mentioned above, requires an incubation time and their combined thickness is less than 1μm. They exhibits an inward growth into the iron substrate, where as the delta phase grows in both directions but generally towards the zinc, which causes the zeta phase to consume the zinc or the eta phase. As the delta phase grows, it consumes the gamma phases and expands into the zeta phase [6]. Consequently, the interface between two phases is not well defined but rather a mixture of the two phases.

The morphology of the zeta phase depends on the iron content in the zinc solution. Zeta grows in a columnar or needle-like morphology adjacent to the delta phase and continues to grow rather than formation of new crystals. However, when the zinc solution is supersaturated with iron, zeta can form as isolated crystals [6].

2.1.2 Factors Influencing Coating Composition

The morphology of the various iron-zinc alloy phases and the appearance of the coating are influenced by a number of factors, including the zinc bath chemistry, substrate steel composition and surface roughness, the time of immersion into the zinc bath, bath temperature, rate of withdrawal from the zinc bath, and the quenching rate. Alloying elements in the steel can act as catalysts for the metallurgical reactions causing rapid formation of the Fe-Zn intermetallic phases. Of particular concern is silicon. While it plays an important role in enhancing the mechanical properties of the steel, when sufficient amount silicon is present, a galvanized coating comprised primarily of Fe-Zn intermetallic phases, as shown in Figure 2-3, is produced. In terms of corrosion resistance in concrete, intermetallic phases are inferior to the eta (η) phase [7]; and hence, less desirable.

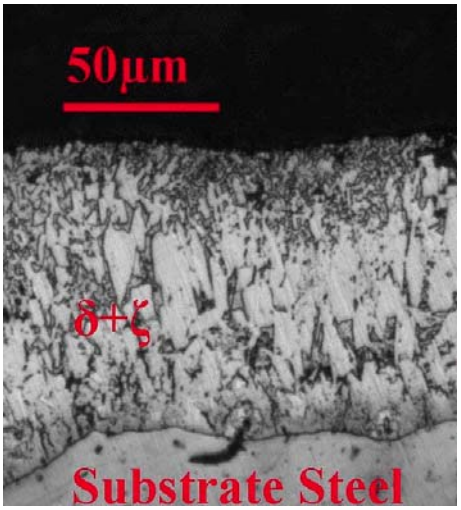

Figure 2-3. Coating containing only Fe-Zn intermetallic phases

The thickness of the resulting coating on silicon-killed steel is more highly sensitive to immersion time than that on unkilled steel. In silicon-killed steel, silicon is added to completely deoxidised the steel to prevent evolution of gas during solidification, leading to a steel that has a high degree of chemical homogeneity and free of porosity. Figure 2-4 illustrate that the coating thickness on silicon-killed steel (with 0.26% silicon) linearly increases with immersion time, where as unkilled steel with residual silicon (of 0.015%) exhibits high initial growth which decreases significantly and gradually reaches a plateau [8].

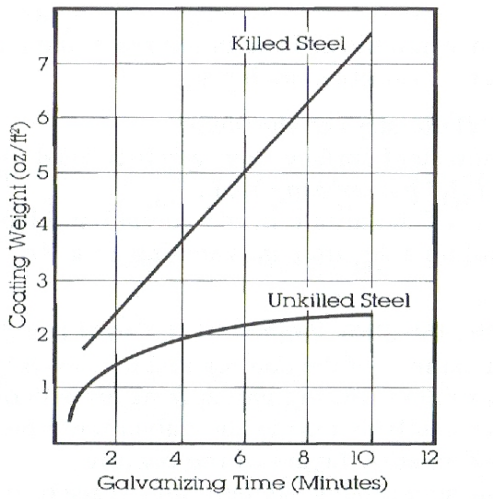

Figure 2-4. Effect of silicon content in steel on galvanizing reaction [8]

In practice, and in many application, a small percentage of aluminium (0.1-0.3 wt%) is added to the zinc bath in order to suppress the reactivity between iron and zinc. As illustrated in Figure 2-5 when sufficient amounts of aluminium are present in the bath, a Fe-Al inhibition layer forms prior to any Fe-Zn reactions, temporarily preventing the formation of the Fe-Zn phases. As a results, a thicker eta layer is formed which has more desirable mechanical properties and corrosion resistance [6]. With time, the inhibition layer becomes unstable and Fe-Zn reactions initiate causing an outburst of Fe-Zn phases as shown in Figure 2-5.

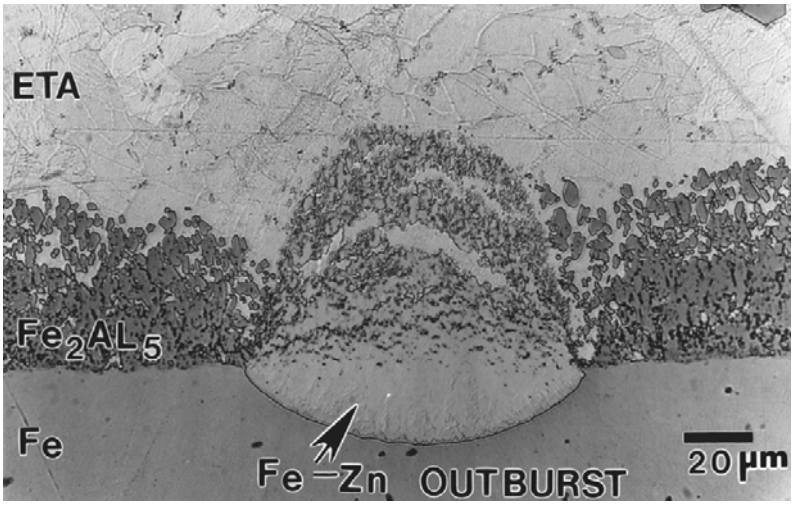

Figure 2-5. Micrograph of Fe-Zn outburst at the Fe-Al inhibition layer [6].

The rate of withdrawal and quenching has a major influence on the microstructure and appearance of the coating. When the withdrawal or quenching is done slowly, more time is allowed for metallurgical reactions to occur, leading to complete consumption of the eta phase. On the other hand, if the steel is withdrawn and quenched quickly the metallurgical reactions can be stopped, leaving a relatively thick eta layer on the surface.

2.2 Corrosion Behaviour of Zinc in Alkaline Environments

In concrete, the pore solution is highly alkaline due to the presence of calcium, sodium and potassium hydroxides. Immediately after mixing, the pore solution is saturated with calcium hydroxide and contains small amounts of sodium and potassium hydroxide giving a pH of at least 12.6 [9]. The pH increases to above 13 within the first several hours and to a maximum of approximately 13.7 as hydration continues. In these conditions, the zinc is thermodynamically

unstable and undergoes vigorously dissolution. This behaviour can be deduced from Figure 2-6, which demonstrates the rapid increase in corrosion rate as pH increase from 12 to beyond 14. The same is also true when pH decreases to a level below 6; however this is not of concern in this study.

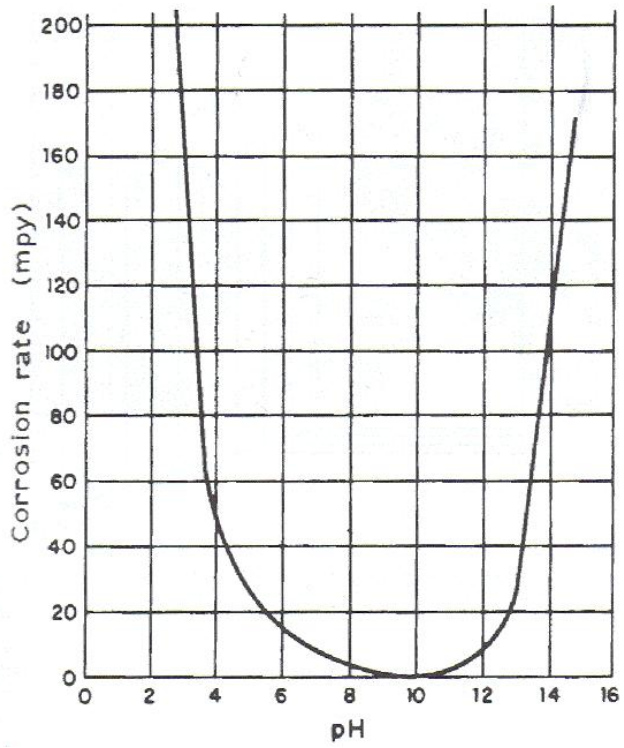

Figure 2-6. Influence of pH on the corrosion rate of pure zinc [10].

In the pore fluid of concrete, zinc corrosion products can react with calcium to form a crystalline material known as calcium hydroxyzincate (CHZ), $Ca(Zn(OH)_3)_2$, which is capable of passivating the zinc from further corrosion. The chemical reactions leading to the formation of the CHZ are complex and not well understood. To date, several mechanisms for CHZ formation have been proposed [11-14], from which Yeoman [9] has provided the following sequence of reactions that appears to best describe the process:

$$Zn + 4OH^- \rightarrow Zn(OH)_4^{2-} + 2e^- \qquad \textbf{Equation 2.1}$$

$$2H_2O + 2e^- \rightarrow 2OH^{2-} + H_2 \qquad \textbf{Equation 2.2}$$

$$Zn + 2OH^- + H_2O \rightarrow ZnO + 2e^- \qquad \textbf{Equation 2.3}$$

$$2H_2O + 2e^- \rightarrow 2OH^{2-} + H_2$$ **Equation 2.4**

$$ZnO + H_2O + 2OH^- \rightarrow Zn(OH)_4^{2-}$$ **Equation 2.5**

$$2Zn(OH)_4^{2-} + Ca^{2+} + 2H_2O \rightarrow Ca(Zn(OH)_3)_2 \cdot 2H_2O + 2OH^-$$ **Equation 2.6**

The degree of passivation provided by the CHZ is, however, highly dependent upon the pH of the solution in which the CHZ is formed. Between pH of 12.5±0.1 and 13.3±0.1 the size of the crystals is sufficiently fine that a continuous and compact layer is formed, protecting the zinc against further dissolution [15]. As the pH increases, the size of the crystals also increases. Beyond pH 13.3±0.1, the size of the crystals is sufficiently large that the zinc surface cannot be completely covered. In some instances, the crystals appear to grow in isolated areas as the calcium content decreases to sufficiently low levels at high pH [15]. The end result is a non-protective layer of CHZ and zinc dissolution continues [15]. Despite the profound influence of pH on the morphology of the CHZ crystals, once a protective layer is formed, further increases in pH up to 13.6 ± 0.1 does not affect its stability and protectiveness [5, 16]. An electron micrograph of the CHZ formed in saturated calcium hydroxide is shown in Figure 2-7.

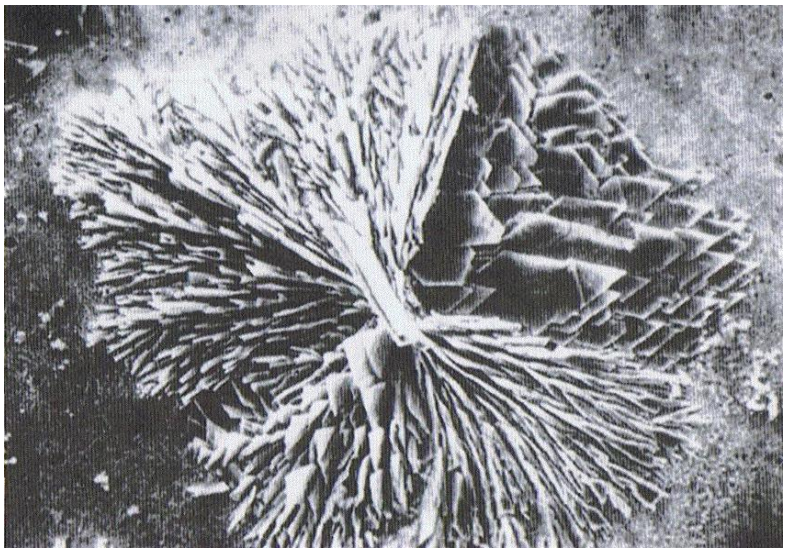

Figure 2-7. CHZ crystal formed in saturated calcium hydroxide solution (160X) [5]

According to Andrade [15], in saturated calcium hydroxide prior to the formation of a passive CHZ layer, the corrosion current is in the range of 10 to 100 μA/cm^2. After approximately two days

of immersion, the passive layer can be formed reducing the corrosion current to negligible levels, i.e. less than 1 μA/cm^2. Adding potassium hydroxide to the solution increases the pH and consequently increases the corrosion rate and time required to form the passive layer.

2.2.1 Hydrogen Evolution

With concrete pore fluid pH being in the range of 12.6 to 13.7, the initial corrosion potential of zinc has been found to be below the hydrogen evolution line [17], line "a" in Figure 2-8. Being below the "a" line, the cathodic half cell reaction is the dissociation of water which produces hydrogen at the interface of the zinc coating and the concrete [18]:

$$2H_2O + 2e^- \rightarrow 2OH^- + H_2 \qquad \textbf{Equation 2.7}$$

For zinc in concrete, the potential at which hydrogen evolution initiates is approximately -0.8 to -0.9V with respect to the standard hydrogen reference electrode or -0.94 to -1.14V with respect to the saturated calomel electrode (SCE). Upon embedment into mortar, potentials have been found to be between -1.4 to -1.5V versus SCE and shifted in the noble direction with time [17].

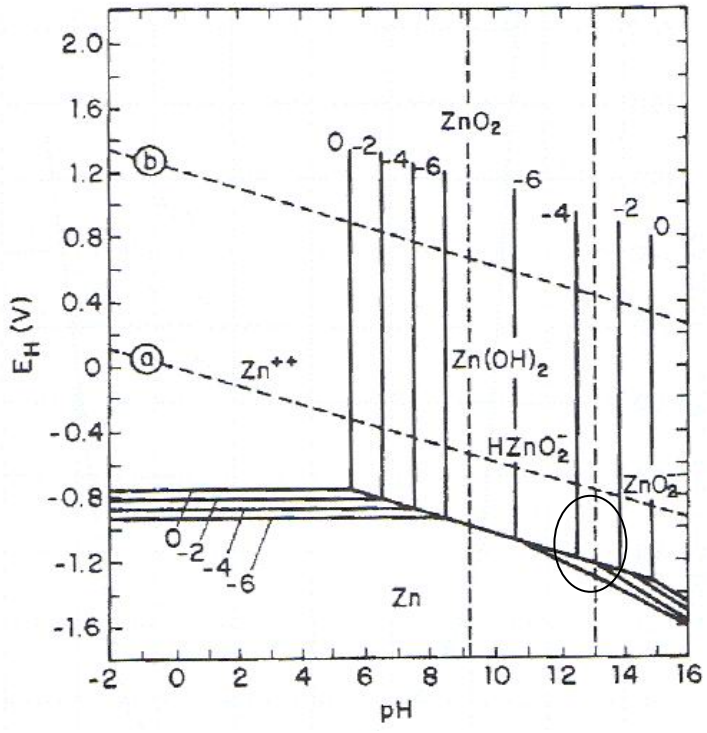

Figure 2-8. Potential/pH diagram of zinc [7]

Previous research has shown that, in mortar, the length of time in which the potential is below the "a" line (hydrogen line) is 1-2 hours [17] as shown in Figure 2-9; however, it is not clear whether or not the potential was monitored immediately after embedment of the HDG bar into the mortar.

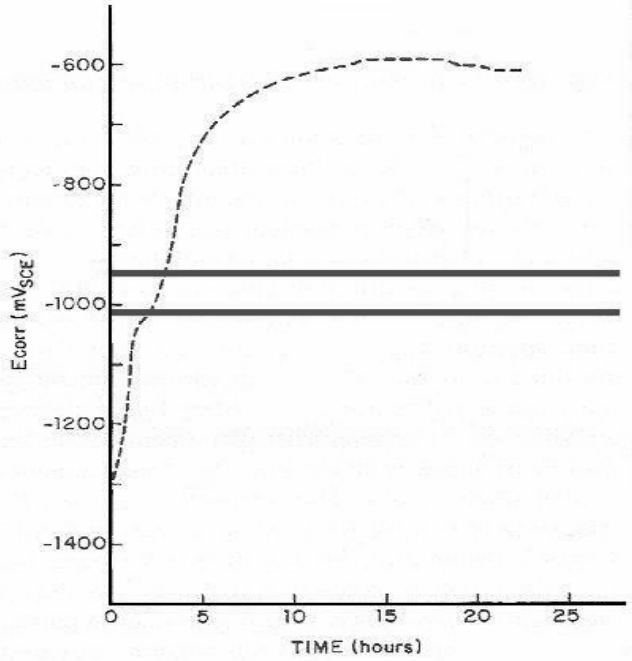

Figure 2-9. Half cell potential profile for galvanized steel embedded in mortar [17]

At potentials above the hydrogen line, the cathodic reaction that occurs is oxygen reduction:

$$O_2 + 2H_2O + 4e^- \rightarrow 4OH^- \qquad \textbf{Equation 2.8}$$

A record of the potential with respect to time is, hence, crucial to determine the type of cathodic reaction that occurs over time, from which the period of hydrogen evolution can be determined. Furthermore, knowledge of the type of cathodic reaction that occurs during corrosion will allow proper determination of corrosion calculation parameters, which will be discussed in conjunction with corrosion techniques.

2.2.2 Effect of Hydrogen Evolution on the Bond between Steel and Concrete

Since hydrogen evolution occurs within the initial few hours of casting into concrete, it is believed to produce additional porosity in the adjacent cement, consequently reducing the contact

area between the concrete and the galvanized rebar, and thus the bond stress. To date, a considerable amount of research has been done in the attempt to clarify this issue through mechanical testing of bond strengths. A detailed summary of the work has been provided by Yeomans [19]. Results of early studies appear to be contradictory.

One study showed that more time is required for full bond development for galvanized rebar than for non-galvanized rebar [1], while another study demonstrated that bond strength is sensitive to surface roughness of the rebar when the rebar is non-ribbed [2]. Compared to rusty, non-galvanized rebar, galvanized rebar showed lower bond strength; however, when compared to clean non-galvanized rebars, galvanized rebars showed higher bond strength.

In recent studies, further clarification has been provided. Kayali and Yeomans [3] performed flexural tests on concrete beams containing black, epoxy-coated, or non-chromated galvanized rebars. The results indicated that there may not be a significant difference in the flexural capacity of the beams regardless of the type of reinforcement when the rib geometry is the same. Subsequently, Kayali and Yeomans [20] conducted additional flexural testing using what is known as the beam-end bond test where both the rebar and concrete are loaded in such a way that represents an actual beam. By continuously monitoring the slippage of the rebar during loading, it was found that 28-days-old specimens showed no significant difference between slippage for the black and galvanized rebars at ultimate load. Similar results have been reported by Belaïd et al. [21] through pull-out tests on smooth galvanized and black rebars: prior to 7 days, the bond strength of galvanized specimens was not significantly different from that of black specimens; however, beyond the 7 day period, a significant increase in bond for galvanized specimens was observed. This increase in bond strength has been postulated to be the effect of CHZ crystal growing into the adjacent cement paste from the rebar-cement interface. It is believed that the CHZ crystals are acting as bridges between the rebar and the adjacent cement, thereby, improving adhesion; hence the bond [22].

Despite these observations, scepticism remains due to the discrepancies in early results and that the work in this area has not been exhaustive. This necessitates further investigation in the present work. In order to further confirm the recent observations, it is necessary to assess the impact of hydrogen evolution in terms of the pore volume it produces at the cement surface adjacent to the rebar.

2.3 The Effect of Chromate Treatment on Corrosion

In the attempt to minimize hydrogen evolution upon embedment into fresh concrete, the galvanized surface is treated with a dilute chromate solution. Treatment is typically done by immersing the galvanized rebar in a chromate solution immediately after withdrawal from the zinc bath. As per ASTM requirements, galvanized steel must be quenched in a solution containing a minimum of 0.2 wt% of sodium dichromate solution or a minimum of 0.2% chromic acid solution. During quenching, a film, with a thickness of 10 to 100nm [23], containing a complex combination of tri and hexavalent chromium [24] forms on the galvanized surface and is believed to provide a combination of a barrier effect and an inhibiting action with respect to zinc oxidation and the associated cathodic reactions [25]. The mechanisms of inhibition of chromate films are complex as they depend on the environment, pH, aggressive ion concentration, etc.; therefore, this is an issue that remains controversial [26].

Limited information is currently available in the literature regarding the effectiveness of the chromate treatment on galvanized steel with respect to corrosion resistance when exposed to alkaline environments. From the work of Short et al. [27], it appears that, despite the treatment, the zinc coating undergoes general dissolution when exposed to highly alkaline solutions. This suggests that the chromate passive layer may not be stable in highly alkaline solutions.

On the contrary, a significant amount of research has been devoted to study the effectiveness of chromate films on corrosion resistance for galvanized steel in environments containing chloride and the general consensus is that chromating improves the corrosion resistance [28-30].

Despite the uncertainty of how well chromate films perform in alkaline environments without chloride, such as that in new concrete, the galvanizing industry generally believes that chromate treatment it is necessary to prolong the life of the zinc coating and maintain the integrity of reinforced concrete.

Currently, the galvanizing industry faces a difficult challenge regarding chromate treatment. Due to the toxicity of hexavalent chromate, its use is being banned in Europe and similar restrictions are being considered in North America. As an alternative method has not yet been developed, the effectiveness and necessity of their use on HDG steel must be elucidated.

2.4 Influence of Coating Surface Condition on Corrosion

The corrosion of the galvanized coating is influenced by its surface condition. A galvanized coating which contains a subsurface of Fe-Zn intermetallic layers and a pure zinc surface layer has been claimed to provide the most effective passivation due to the high availability of zinc on the surface [7]. Figure 2-10 illustrates the nature of dissolution of the pure zinc layer during passivation.

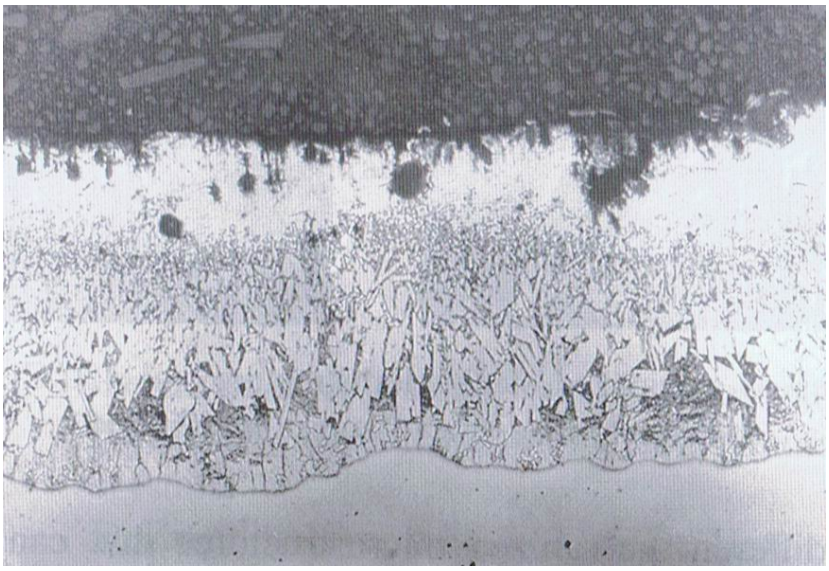

Figure 2-10. Dissolution of pure zinc surface layer during passivation [7]

For annealed coatings, which lack the pure zinc surface layer, the Fe-Zn intermetallic layers are less stable and, during corrosion, zinc is selectively dissolved causing the coating to disintegrate as illustrated in Figure 2-11.

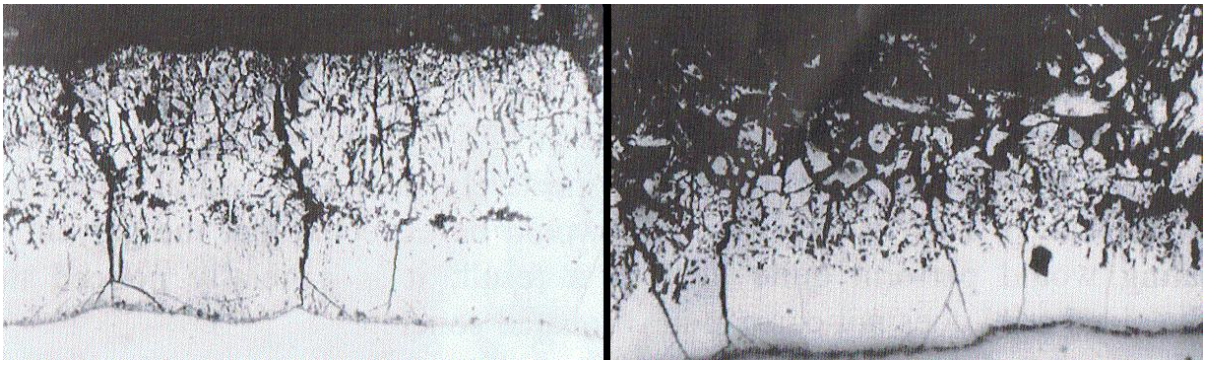

Figure 2-11. Selective dissolution of zinc in Fe-Zn intermetallic layers [7]

Despite observations of this type, it remains unclear whether or not the degree of corrosion protection is compromised. While on one hand it has been reported that annealed bars exhibit higher corrosion rates than non-annealed bars in OPC mortar, Figure 2-12, on the other, similar type of bars were shown to exhibit significantly lower corrosion rates as shown in Figure 2-13.

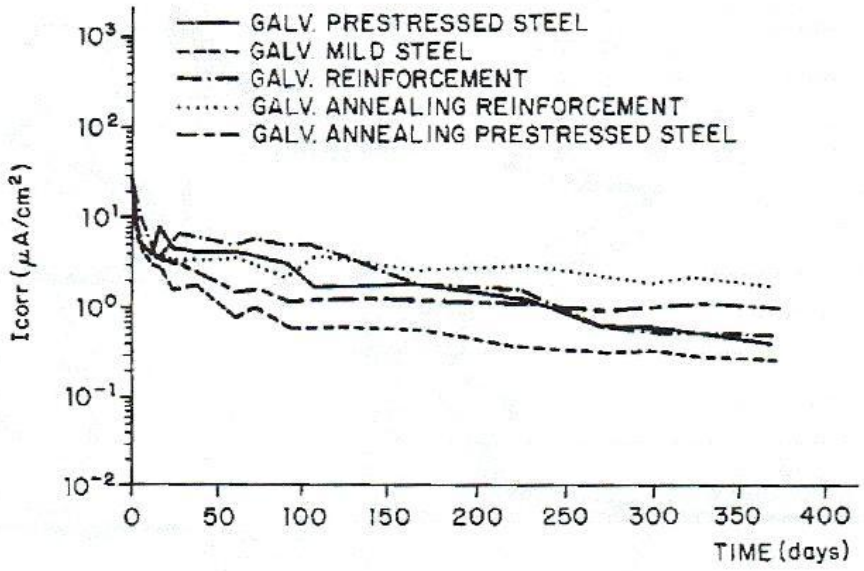

Figure 2-12. i_{corr} of galvanized and galvannealed steel [7]

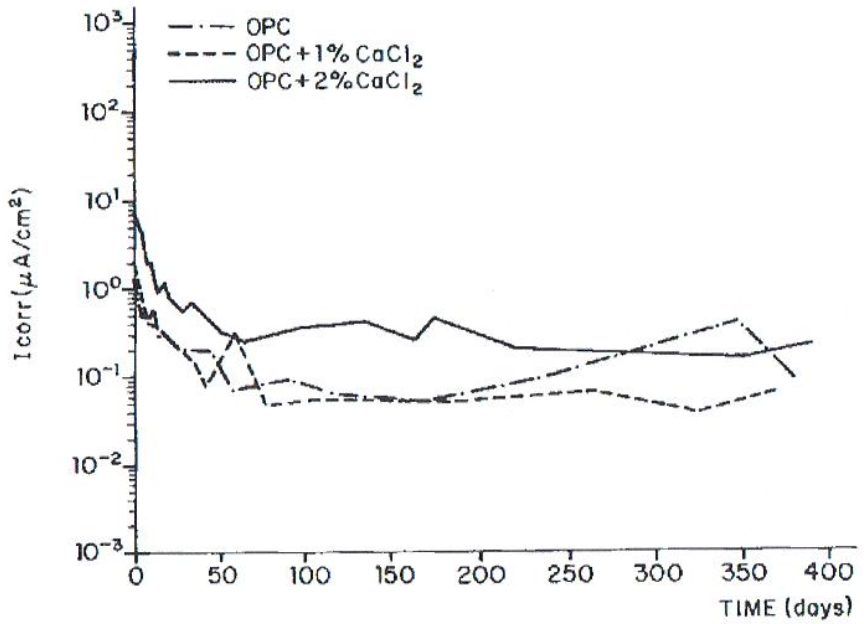

Figure 2-13. i_{corr} of galvanized steel without the eta layer embedded in cement mortar [7]

From these observations, the importance of coating surface condition on corrosion is highlighted and elucidates that research is required to study the influence of other surface conditions. Of particular concern to the galvanizing industry is how corrosion is influenced by chromate treatment and exposure to weathering that causes the surface zinc to oxidize and carbonate.

2.5 The Influence of Supplementary Cementing Material on Corrosion

Supplementary cementing materials such as silica fume and ground granulated blast furnace slag (GGBFS) are commonly used as partial replacements of ordinary Portland cement (OPC) in concrete to improve strength and durability by reducing the volume of porosity and increasing the amount of calcium silicate hydrate (C-S-H), the hydration product that provides strength to concrete. However, upon hydration, silica fume and GGBFS consume alkalis, hence, the final pH of the concrete pore fluid can be decreased. Since the corrosion behaviour of zinc in concrete is highly dependent on the pH of the pore fluid, it may be influenced by silica fume and GGBFS. Furthermore, differences in the particle fineness and chemical composition of silica fume and GGBFS from ordinary Portland cement also influence the rate of cement hydration, and hence, the pH development and ionic concentration of the pore fluid. Therefore, literature regarding these matters was explored and a brief summary is provided in this section. Prior to discussing hydration mechanisms of silica fume and GGBFS, it is essential to first describe the basic hydration of ordinary Portland cement.

2.5.1 Hydration of Ordinary Portland Cement Concrete

The four main components of OPC are: tricalcium silicate ($3CaO{\cdot}SiO_2$ or C_3S), dicalcium silicate ($2CaO{\cdot}SiO_2$ or C_2S), tricalcium aluminate ($3CaO{\cdot}Al_2O_3$ or C_3A) and tetracalcium aluminoferrite ($3CaO{\cdot}Al_2O_3{\cdot}Fe_2O_3$ or C_4AF). Minor components of cement include K_2O, MgO, TiO_2, Mn_2O_3, and Na_2O. In addition, sulphate in the form of gypsum is added to OPC to react with C_3A to prevent a phenomenon known as flash set, where the cement sets rapidly. When sulphate is present, it reacts with C_3A to form ettringite which temporarily coats cement grains to prevent rapid hydration. The calcium silicates, C_2S and C_3S, makes up approximately 75% by mass of the cement. Upon hydration, they produce calcium hydroxide and C-S-H, which contributes to the pH of the pore solution and strength of the concrete, respectively. Upon mixing with cement, the water immediately becomes saturated with calcium hydroxide and high concentrations of sodium and potassium hydroxide. Values 13 to 13.2 for pH have been documented for freshly mixed ordinary Portland

cement concrete; with further hydration the final pH reached is approximately 13.7 due to additional release of sodium and potassium hydroxide into the pore solution[31].

2.5.2 Influence of Silica Fume on Concrete pore Chemistry and pH

Silica fume is a by-product of silicon and ferrosilicon alloy production. The fineness of silica fume particles is about 100 times smaller than that of cement particles and their composition is more than 90% SiO_2.

Although, information on the hydration of cement containing silica fume is limited, the work by Larbi et al.[31] clearly demonstrated the effect of silica fume on the hydration of cement, particularly, the development of pH and calcium content of the pore solution of concrete. OPC cement without and with 20% replacement by silica fume was hydrated up to 28 days, and the pore solution was extracted at various times for chemical analysis. Between 4 to 24 hours of hydration, blended cement displayed significantly higher pH compared to plain OPC cement mix. The effect appeared to be more pronounced at lower water to binder (w/b) ratios. At a w/b ratio of 0.45, the pH after one day of hydration was greater than 13.4. At this pH, as discussed earlier, the corrosion rate of zinc is high and passivation may not be possible. At w/b ratio of 0.40, the pH reached approximately 13.7 between 4 to 24 hours. The trend of Na^+ and K^+ was in agreement with the pH trend, with sharp increase from about 4 hours to 24 hours.

The pore solution calcium content for the blended cement was found to be significantly lower than that of OPC. More than 80% of the calcium release during the onset of hydration was consumed after 4 hours. The author believed this to be a result of higher pH in blended cement which causes the calcium and silicon to react immediately to form calcium silicate hydrates, and consequently, decreases the amount of calcium in the pore solution.

2.5.3 Influence of Ground Granulated Blast Furnace Slag on Cement Hydration

Ground granulated blast-furnace slag (GGBFS) is a by-product of smelting of steel, collected in a form of aggregates which are then ground to the same fineness as Portland cement. The primary components of GGBFS are SiO_2, MgO, and Al_2O_3.

While it is known that GGBFS in Portland cement improves strength and reduces permeability[32], its effect on pore solution chemistry, particularly, the calcium content and pH development during the initial few days of hydration has not been documented.

Chapter 3
Experimental Work

3.1 Materials

3.1.1 Galvanizing

The galvanized rebars were prepared by Pure Metal Galvanizing, Mississauga, ON and Galvcast Manufacturing Inc. Acton, ON. Uncoated, deformed carbon steel bars were cut to 305 mm lengths and cleaned in a caustic bath to remove organic contaminants. After rinsing with water, the bars were pickled in dilute sulphuric acid to remove all oxidation products, rinsed again with water and immersed in a zinc ammonium chloride solution for fluxing. After drying, the bars were dipped into a molten zinc bath at a temperature between 450°- 490^{o}C for approximately 2 minutes. To achieve the desired composition for chromated and non-chromated bars, one set of 10 HDG bars was quenched immediately in a 1.2% chromic acid solution and two sets were quenched in a water bath. The rapid quenching process limited the time for alloying between zinc and the underlying steel and resulted in a layer of relatively pure zinc (eta (η) phase) at the surface of the galvanized coating. One set of the non-chromated bars was subsequently placed outdoors and allowed to "weather" for several months.

For the "annealed bars", a fourth set of hot-dipped bars was centrifuged and then quenched in a cold water bath. The centrifugal action removed excess molten zinc and allowed additional time for intermetallic diffusion to occur, consequently, forming Fe-Zn intermetallic phases throughout the entire coating.

In the present work, the initial corrosion of four types of HDG steel has been evaluated:

1. HDG rebar with a pure zinc surface layer and iron-zinc alloy subsurface layers (hereafter referred to as "non-chromated bar"),
2. HDG rebar with a coating containing only Fe-Zn alloy layers (hereafter referred to as "annealed bar" after its microstructural similarity to annealed galvanized steel),
3. HDG rebar with a pure zinc surface layer exposed outdoors to produce a layer containing zinc oxide and zinc carbonate (hereafter referred to as "weathered bar"),

4. HDG rebar with a pure zinc surface layer and a chromate surface film applied through immersion in a dilute chromic acid solution (hereafter referred to as “chromated bar”).

3.1.2 Microstructural and Composition Analysis of Coatings

Cross-sections of samples of each type of bar were mounted in epoxy, ground, and polished to remove scratches and then etched with a 2% Nital solution to reveal the microstructure of the coating. Optical microscopy of the specimens was used to assess the uniformity and thickness of the coating. Using a Scanning Electron Microscope (SEM) with Energy Dispersive x-ray Spectroscopy (EDS), the compositions of the various iron-zinc phases within the coating were confirmed.

For the weathered coatings, the surface composition was confirmed using Raman spectroscopy (RS), a technique used to analyze materials by means of obtaining spectra unique to the molecular structure that makes up a material. A Raman spectrum is obtained by irradiating a material with monochromatic radiation, ranging from visible to near infrared. Incident radiation, upon contact with molecules is scattered, with a minute fraction of the scattered light shifted in wavelength as a result of interaction with vibrating molecules. As the wavelength change is unique to a molecular vibration, the collection and analysis of the wavelength change of the radiation reveals the chemical composition of the analyte. The collected data is in the form of a spectrograph where the vertical axis is the relative intensity of a spectrum with obituary units, and the horizontal axis is the Raman shift, or a measure of energy shift of light in wave-number (the inverse of frequency). Each peak is associated with a specific mode of vibration of a molecule. The peaks are then identified by matching spectra of materials with known composition.

3.2 Corrosion Environments and Setup

The bars were tested in both alkaline solutions and in concrete. The compositions of the solutions are given in Table 3-1, and the cement compositions in weight percents and the mixture proportions per cubic meter of the concrete are given in Table 3-2 and Table 3-3, respectively. The type 10E-SF cement used for the silica fume concrete contains approximately 8 wt% cement replacement by silica fume. For the slag concrete, 25 wt% of the type 10 cement was replaced by slag.

Table 3-1. Composition of solutions

pH	$Ca(OH)_2$ (M)	KOH (M)	NaOH (M)
12.5	Saturated	---	---
13.3	0.016	0.11	0.05
13.5	0.016	0.22	0.07
13.7	0.016	0.40	0.13

Table 3-2. Chemical composition of cements in weight percents

	Type 10	Type 10E-SF	Slag
SiO_2	19.6	22.5	40.69
Al_2O_3	4.8	4.6	7.89
Fe_2O_3	3.1	3.0	0.57
Total CaO	60.5	55.5	38.93
MgO	2.4	2.2	11.16
SO_3	4.0	3.9	2.25
Na_2O equivalent	0.9	1.0	0.9

Table 3-3. Concrete mix proportions in kg/m^3

Component	OPC Concrete	Silica Fume Concrete	Slag Concrete
Cement	390 kg type 10	390 kg type 10E-SF	292 kg type 10 + 98 kg slag
Coarse aggregate (≤ 7 mm)	1100	1100	1100
Fine aggregate	735	735	735
Water	176	176	176
Air entraining agent	60 mL/100 kg of cement	60 mL/100 kg of cement	60 mL/100 kg of cement

Two types of cylindrical concrete specimen were used. In the first, illustrated in Figure 3-1, the cylinder was 150 mm ø by 300 mm and one bar of each surface condition was placed at an equal distance from a Mn/MnO_2 reference electrode, located centrally in the cylinder. The bars were

partially painted with epoxy to allow an exposed length of 64 mm. A cylindrical stainless steel sheet with a length of 64 mm was used as counter electrode. Three identical cylinders were prepared for replicate measurements.

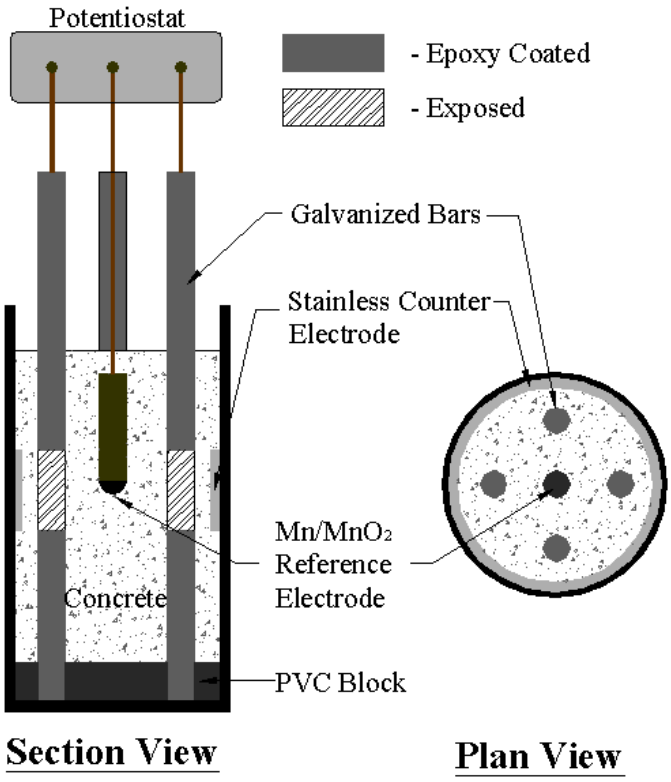

Figure 3-1. Schematic diagram of specimens for monitoring corrosion current and potential

Figure 3-2a and b illustrate the experimental setup used for corrosion monitoring of the bars in solution and concrete, respectively. In this case, the cylinders were 100 mm ø by 200 mm. The HDG bar and graphite counter electrode were partially painted with epoxy to give the same exposed length allowing the exposed zinc surface to be uniformly polarized. The graphite "reference electrode" was partially painted to give a smaller exposed area, as shown, to minimize fluctuation in its potential. The electrodes were positioned 10 mm away from the HDG bar; this distance is greater than the maximum aggregate size of 7 mm to ensure free flow of concrete during casting and compaction to prevent damage to the electrodes by aggregates.

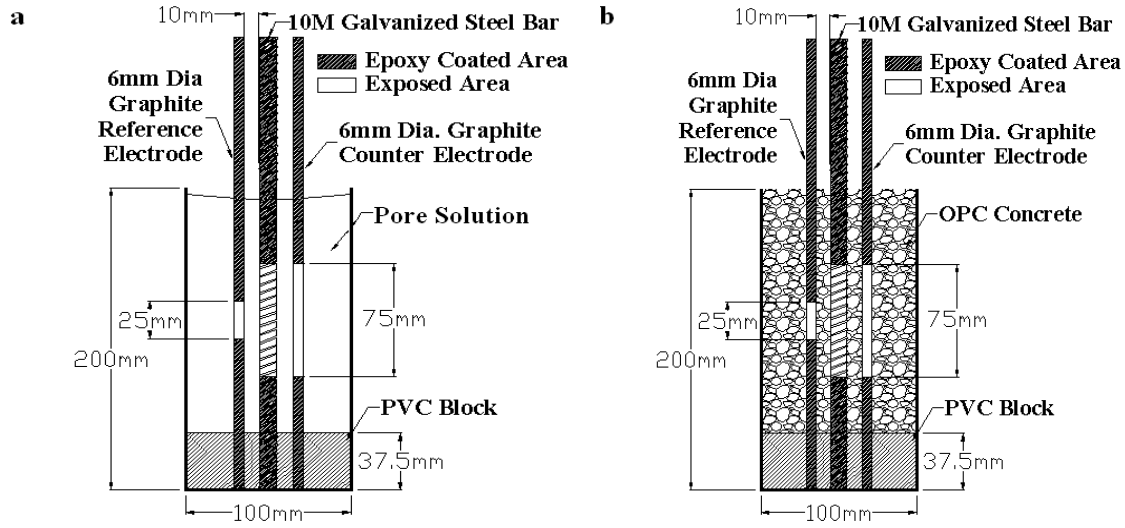

Figure 3-2. Experimental set up for monitoring the corrosion behaviour of the bars in (a) solutions of different pH and (b) concrete

3.3 Identification of Calcium Hydroxyzincate

The primary purpose of the solution experiment was to obtain the CHZ and standardize its composition and, therefore, only one of each of the non-annealed, annealed and chromated bars was immersed in each type of solution. The weathered specimens were not available at the time of testing.

By observing the corrosion in the solutions with varying pH, the morphology of the CHZ formed was assessed. More importantly, the CHZ could be extracted and analysed. The bars were immersed in solutions in Table 3-1 for several days to allow sufficient amounts of CHZ to form on the surface. Upon withdrawal from the solution, the CHZ crystals were carefully extracted to avoid contamination. In order to analyse the CHZ crystals with X-ray diffraction (XRD), they were ground to a fine powder and kept in a vacuum to avoid oxidation and carbonation prior to testing. Using XRD, the composition of the CHZ was confirmed. In light of better understanding the data, a brief description of the principal of XRD is provided here.

Crystalline materials contain unique arrays or planes of molecules, atoms or ions. X-rays, having wavelengths in the order of the interplanar spacing of crystalline materials can get diffracted at specific incidence angles upon interaction with a crystalline material. When a beam of monochromatic x-rays is incident on two planes of atoms with a particular interplanar distance, the x-

rays can get scattered in such a way that constructive interference or diffraction will occur. An x-ray detector then collects the diffracted x-rays and measures the intensities at an angle 2θ from the incident x-rays as shown in Figure 3-3. The detector, labelled "c", and the specimen, labelled "s", rotate simultaneously to maintaining the $\theta/2\theta$ relationship, in order to record all angles at which diffraction occurs. Since diffraction occurs at unique angles for a particular crystal material, a plot of the 2θ and relative intensities of the diffracted x-rays, known as diffraction pattern, is then used for identification of crystalline material. To identify an unknown material, matching of diffraction patterns from known materials is performed.

By grinding the specimen into a powder, each particle of the powder is presumably a crystal or a minute amount of crystals. By doing so, a crystalline material would have all its lattice planes randomly distributed hence maximize the probability of correct orientation between the lattice planes and the incident ray at which diffraction would occur.

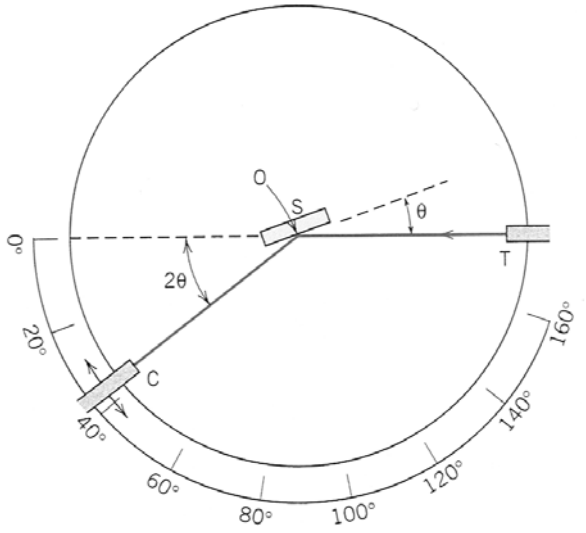

Figure 3-3. Theoretical arrangement of an x-ray spectrometer [33]

Since XRD patterns for CHZ already exist in the literature, by first confirming the composition of the CHZ powder with XRD, Raman spectroscopy was subsequently used to analyse the same powder in order to obtain a Raman spectrum which could be used as a standard. Since Raman spectroscopy can be used to conduct in situ analysis of materials, any CHZ formed of corroded HDG bars can be confirmed using the obtained standard.

3.4 Corrosion Monitoring

3.4.1 Linear Polarization Resistance

Corrosion monitoring was achieved using potentiostatic linear polarization resistance (LPR), a technique widely used for measuring corrosion rates both in the field and laboratory. The key advantages of LPR over other techniques stem from its rapidity of measurement and the proximity of the applied potential to the open circuit potential of a corroding metal. During a LPR measurement, the surface of the corroding metal is not significantly disturbed since the reactions that occur during measurement do not differ from those that occur in the natural state. This allows measurements to be done at frequent intervals, as very little time is required for depolarization of the corroding metal. The rate of corrosion can be determined in matter of a few minutes, making LPR an excellent technique for determining instantaneous corrosion rates.

For potentiostatic LPR, the rebar was polarized by an externally applied potential, ±20mV from the open circuit potential, and the current response was measured. The potential was first applied in the cathodic direction for 150 seconds to allow the resulting current to reach a steady state. Subsequently, the potential is applied in the anodic direction for 150 seconds. To determine the polarization resistance (R_p), the is the resistance of the metal to oxidation, the difference in applied potential is divided by the difference in the resultant current:

$$R_p = \frac{\Delta E}{\Delta I} \qquad \textbf{Equation 3.1}$$

Where ΔE and ΔI are the difference in potential and current respectively. The corrosion rate i_{corr}, which is inversely related to R_p can be then calculated using the Stern-Geary equation [34]:

$$i_{corr} = \frac{\beta_a \cdot \beta_c}{2 \cdot 3(\beta_a + \beta_c) \cdot A} \cdot \frac{\Delta I}{\Delta E} = \frac{B}{A \cdot R_p} \qquad \textbf{Equation 3.2}$$

where A is the corroding area, and β_a and β_c are the anodic and cathodic Tafel constants respectively. These parameters are determined experimentally through potentiodynamic polarization. B is a constant that is a function of β_a and β_c. While the B values for uncoated carbon steel rebar in concrete have been established, there are discrepancies in the values for HDG steel. In synthetic concrete pore solution, values of 13mV and 52mV for active and passive corrosion have been cited, while in mortar, depending on exposure conditions, the values vary greatly in the range of 13 to 62mV [15, 35].

From i_{corr} the depth loss of zinc can by calculated based on Faraday's Law [36]:

$$D = \frac{i_{corr} ta}{nF\rho} \qquad \textbf{Equation 3.3}$$

where t is the time (s), a is the atomic weight (g/mol), n is the number of equivalents exchanged, F is the Faraday's constant (96,500 coulombs/equivalent) and ρ is the density of Zn in g/cm3.

In order to determine I_{corr} from LPR with reasonable accuracy, the Tafel constant must be accurately determined by performing cyclic polarization, which is discussed below.

3.4.2 Determination of Tafel Constant and Corrosion Monitoring

By measuring the polarization resistance, R_p, the corrosion current density i_{corr} was calculated using the Stern-Geary. The β values for active and passive corrosion were determined by performing cyclic polarization scans. For the active case, the HDG bar was immersed in the synthetic pore solution with a pH of 13.5 in Table 3-1 and polarized from the open circuit potential, E_{corr}, to 300mV more cathodic than E_{corr} then the potential was reversed to 300mV more anodic than E_{corr}. A 0.1 mV/s scan rate was chosen so that the time required from start to finish is sufficiently short that the system does not change significantly as zinc corrodes.

For the passive case, the HDG bar was immersed in the solution for 3 days to allow passivation to occur prior to performing the polarization scan. To avoid reduction of the passive CHZ layer, the potential was first applied in the anodic direction, 300mV more positive than the open circuit potential then reversed to 600mV more negative.

The anodic curve did not display as well a defined linear region as the cathodic curve. For this reason, the anodic Tafel line can then be calculated as the difference between the cathodic Tafel line and the measured net current [36]:

$$i_a = i_{meas} - i_c \qquad \textbf{Equation 3.4}$$

Where i_{meas}, i_a, and i_c are the measured (net), anodic, and cathodic currents respectively. By calculating i_a at numerous potentials, the anodic Tafel line and constant β_a was approximated.

In order to use the appropriate B value, it is necessary to ascertain the cathodic half cell reactions occurring at different stages of the corrosion of the bars in concrete. The potential/pH

diagram in Figure 3-4 illustrates that, for zinc in concrete, with a pH of ~13.5, the potential at which hydrogen evolution discontinues and oxygen reduction becomes the cathodic half cell reaction during corrosion is approximately 0.9 V versus the standard hydrogen electrode or 1.1 V versus the saturated calomel electrode. Using the setup as shown in Figure 3-1, the corrosion potential and current of HDG bars embedded in concrete were monitored using LPR at 20 minute intervals for the initial two days to determine:

1. the correlation between the corrosion current and potential;
2. the corresponding cathodic reaction that occurs during active and passivate corrosion;

After ascertaining the cathodic reactions for active and passive corrosion from the potential data, and the corresponding B values, the i_{corr} and depth loss of zinc were calculated.

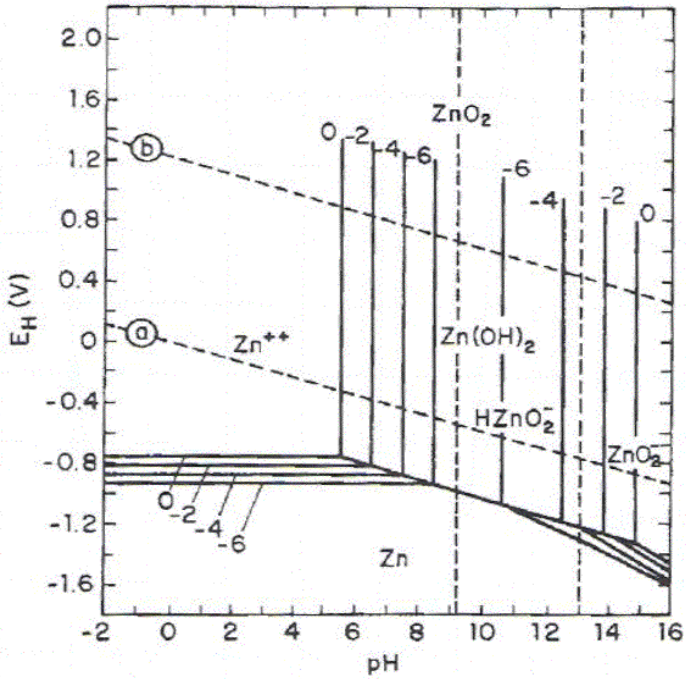

Figure 3-4. Potential/pH diagram of zinc [7]

To determine the effect of coating surface composition on corrosion, five ordinary Portland cement concrete specimens of the type shown in Figure 3-2b were cast for each type of HDG bar and uncoated carbon steel bars as controls. On the other hand, for the purpose of assessing the influence of silica fume and slag on corrosion, five concrete specimens were cast only for the chromated and non-chromated HDG bars. By incorporating the chromated bars, the effect of chromated treatment on

corrosion can be assessed amongst the different concrete mixtures. Immediately after immersing or embedding the bars in solution and in concrete, corrosion was monitored using LPR at hourly intervals for the initial two days.

3.5 Autopsy of Corroded Rebars

After corrosion monitoring using cylinders represented by Figure 3-2b, the specimens were autopsied. Photographs of the rebars were taken to illustrate any difference in surface appearance. More importantly the rebars were analysed using Raman spectroscopy to detect the presence of calcium hydroxyzincate and any difference in its concentration amongst the rebars.

3.6 Monitoring of pH Development in Different Concrete Mixes

Since the corrosion rate of zinc is directly influenced by the pH of the concrete pore fluid, it was considered crucial to monitor its development in the different concrete mixes used in the present work. By doing so, any deviation in corrosion behaviour for different concrete types could be correctly interpreted.

In the present work, pH was determined by measuring the potential difference between a pH electrode and reference electrode in solutions with known pH. Then the potentials, measured in the same manner, in concrete were used to determined pH.

3.6.1 Preparation of pH Electrodes

In order to accurately measure pH, a pH and reference electrode with high stability and response time is required. In the present work, Ir/IrO_2 electrodes and saturated calomel electrodes (SCE) were used as the pH and reference electrode respectively. The SCE electrode is commercially available and has high potential stability and fast response time. Commercially available pH electrodes were not used because their glass tip and body are prone to dissolution in highly alkaline environments during long exposures; thereby, leading to erroneous readings. This limitation is eliminated by using Ir/IrO_2 pH electrodes, which can be permanently embedded into concrete. These electrodes were constructed based on the work of Du et al. [37], where it has been shown to be suitable for longer term pH monitoring in concrete.

High purity (99.99%) iridium wires (0.3 mm diameter) were cut to 10 mm lengths and subsequently heat treated for approximately 1 hour at 700 ^{o}C while embedded in Na_2CO_3 powder.

The heat treatment allowed a layer of IrO_2 to form on the surface. Upon cooling, the Ir/IrO_2 wires were spot welded to 15 cm long copper core wires with 1 mm diameter. To ensure high stability and fast response time, the electrodes were immersed in the solution with a pH of 13.8 in Table 3-4, to hydrate the IrO_2 layer. The solution was renewed at seven day intervals for at least 30 days prior to using the electrodes.

Table 3-4. Composition of buffer solutions

pH	$Ca(OH)_2$ (M)	NaOH (M)	KOH (M)	$CaSO_4$ (M)
12.8	0.016	0.008	0.023	0.142
13	0.016	0.017	0.051	0.142
13.3	0.016	0.037	0.111	0.040
13.5	0.016	0.072	0.216	0.009
13.8	0.016	0.130	0.400	0.007
14	0.016	0.242	0.726	0.007

The experimental setup used for calibration is shown in Figure 3-5a. The Ir/IrO_2 electrodes were immersed into solution with known pH in Table 3-4, and the potential difference versus SCE was recorded. The pH of the solutions was confirmed through potentiodynamic titration to be within ±0.1 of the theoretical pH as shown in Table 3-5.

Table 3-5. Comparison of theoretical and titrated pH

Theoretical pH Values	Titrated pH Value
12.5	12.5
12.8	12.9
13	13.1
13.3	13.2
13.5	13.4
13.8	13.7
14	13.9

To avoid damaging the SCE electrode, it was immersed in a saturated solution of KCl which is separated from the alkaline solution by an agar gel salt bridge. A similar setup, Figure 3-5b, was used to monitor the potential in concrete. Using the calibration data, the potentials measured in concrete were converted to pH through linear interpolation.

Three specimens of each concrete type in Table 3-3 were monitored to ensure representative results were obtained.

After observing fluctuations in the pH of OPC concrete, during the subsequent monitoring of silica fume and slag concretes, temperature development was monitored by embedding a thermister in the concretes. This was aim to identify any correlation between the measured potential and temperature.

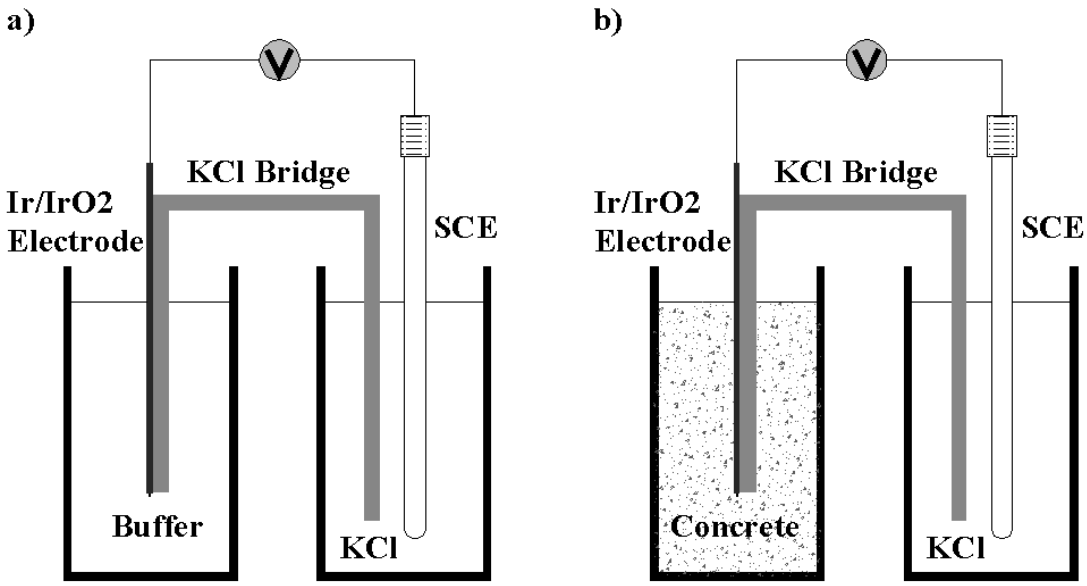

Figure 3-5. Schematic of a) electrode calibration b) pH monitoring

3.7 Concrete Resistance Monitoring

As concrete resistance has direct influence on measured current and potential, monitoring its development over time may help the interpretation of measured potential for pH monitoring and the corrosion current determined from LPR. To monitor concrete resistance, a galvanostatic pulse technique was employed. Figure 3-6 is a schematic of the experimental setup used. The working electrode is polarized by applying an anodic 400μA current pulse from the counter electrode. The resultant polarization is measured with respect to the reference electrode and plotted against time as illustrated schematically in Figure 3-7. When the current pulse is applied to the system, an immediate increase in potential occurs due to the ohmic resistance of the concrete and the subsequent gradual increase is due to polarization resistance of the working electrode. The resistance of the concrete was calculated by dividing the initial potential increase by the applied current. For a complete scan, the

duration of polarization is typically 1 to 20 seconds; however, since only the ohmic resistance is of interest, one-second duration was sufficient. Using this technique, the resistance of three specimens of each type of concrete in Table 3-3 was monitored at 30 minute intervals for 48 hours. The 30 minute interval was chosen to allow the working electrode to depolarize in between measurements.

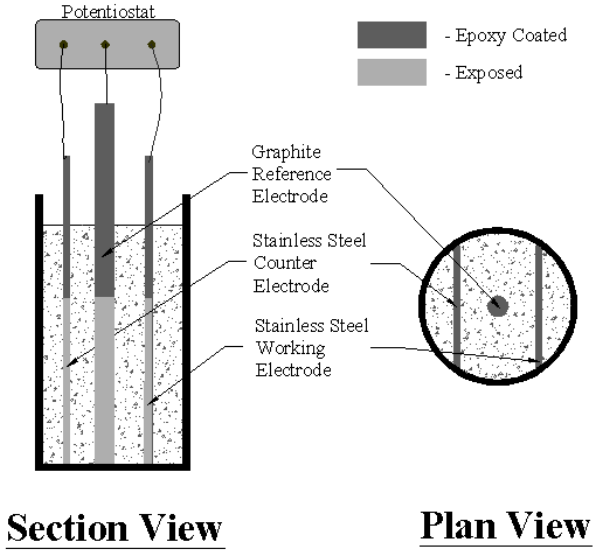

Figure 3-6. Schematic diagram of concrete resistance measurement setup

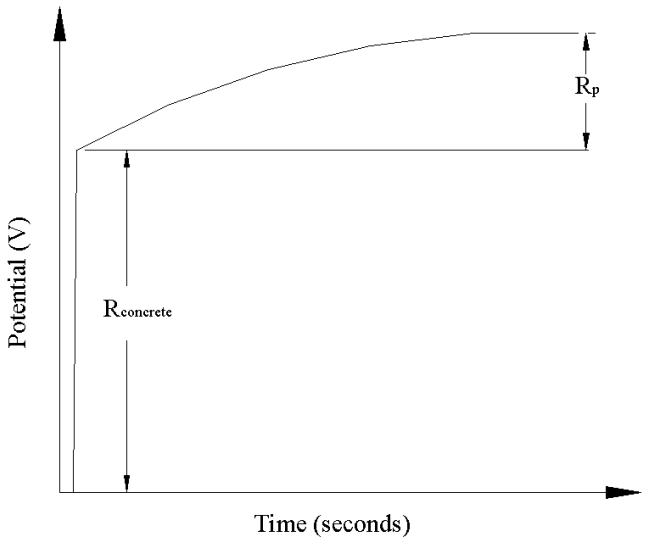

Figure 3-7. Plot of potential versus time from galvanostatic pulse technique

3.8 Mercury Intrusion Porosimetry

To assess the impact of hydrogen evolution and the effectiveness of chromating in minimizing it, the porosity of cement paste adjacent to both chromated and non-chromated galvanized rebars was determined using mercury intrusion porosimetry (MIP). The technique is based on the principle that mercury, a non-wetting liquid, will intrude a pore of a certain radius under sufficient pressure. Hence, by forcing mercury into hydrated cement or mortar at a controlled increasing rate of pressure, the radii and volume of total pores intruded can be determined. The relationship between pore radius and applied pressure is given by the Washburn equation:

$$r = -\frac{2\gamma \cos\theta}{P} \qquad \textbf{Equation 3.5}$$

Where r is the pore radius, P is the applied pressure, γ is the surface tension of the mercury, and θ is the contact angle between the mercury and the pore wall. The volume of intrusion is calculated directly from volume of mercury intruded.

3.8.1 Specimen Preparation

Cylinders of cements in Table 3-3 were cast, with each type containing chromated and non-chromated rebar. As a control, an ordinary Portland cement cylinder was cast with an embedded uncoated black rebar. After hydrating in a laboratory environment for nine days, the cylinders were demoulded and split without damaging the cement face adjacent to the rebar. Specimens of the dimensions given in Figure 3-8 were cut out from the cylinders using a diamond saw. Each specimen was weighed and then submerged into isopropyl alcohol for 24 hours, allowing water in the cement pores to be replaced. The specimens were then withdrawn from the alcohol and put under a vacuum to allow the alcohol to evaporate. As the weight of the specimens was stabilized when evaporation was complete, the process was repeated until the weight of the specimens remained constant. Prior to performing MIP, the specimens were kept in a vacuum dessicator containing desiccant to prevent further hydration of the specimens. Three specimens from each cylinder were prepared and tested using MIP.

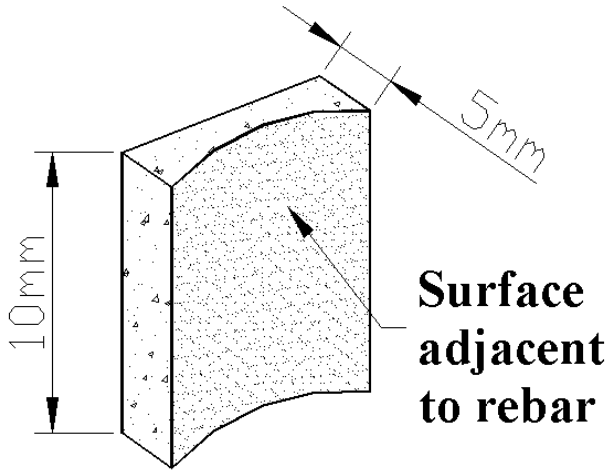

Figure 3-8. Cement specimen for mercury intrusion porosimetry

3.9 Microscopy of Cement Adjacent to Rebar

To provide further clarification to the impact of hydrogen evolution, cement specimens prepared in same manner as that in Figure 3-8 were mounted in epoxy and polished to allow analysis using an environmental scanning electron microscope (ESEM) with energy dispersive x-ray spectroscopy (EDS) capability. The advantage of using an ESEM is that the environment in which the sample is located has high relative humidity which can provide the conductivity needed for non-conductive samples such as cement. This eliminates the need to coat the samples with gold or carbon to achieve conductivity that is required for imaging.

Using the EDS, the elemental composition of a sample or a small area of that sample can be determined. During EDS, the same electron beam used for ESEM imaging collides with electrons of the sample, which causes some of them to be knocked out of their orbits. The electron vacancies are then replaced by higher energy electrons that emit x-rays. By collecting and analyzing the emitted x-rays the elemental composition of the area being analysed can be determined. Once an image was obtained using ESEM, EDS was used to trace the zinc content from the cement/rebar interface into the cement paste. Since the zinc is indicative of presence of zinc corrosion products, the depth at which these products diffuse into the cement was measured.

Chapter 4
Results and Discussion

4.1 Coating Microstructure and Composition

Shown in Figure 4-1 are optical micrographs of HDG bar cross-sections. From optical microscopy, the thickness of coatings for all bar types generally ranged between 100 to 350 μm.

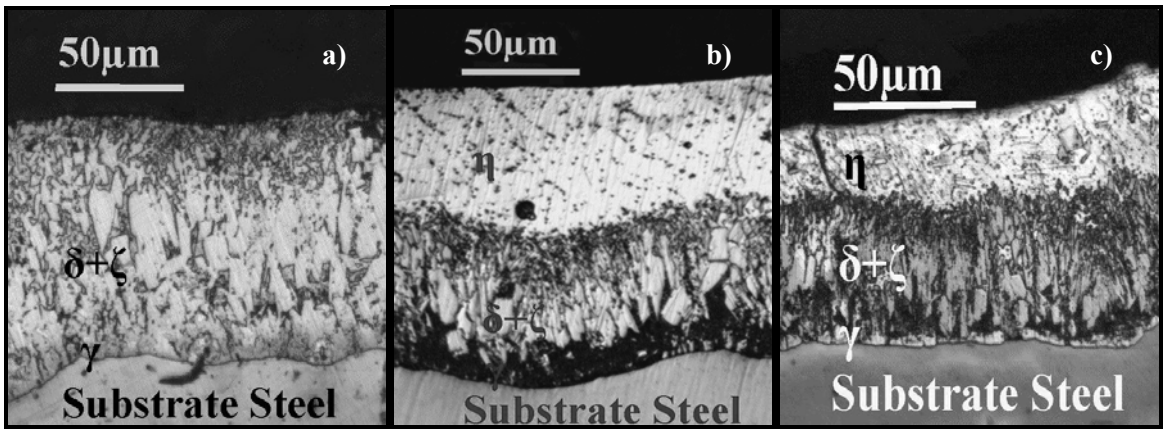

Figure 4-1. Cross section of a) annealed b) non-chromated and c) chromated coating

Using a Scanning Electron Microscope (SEM) with Energy Dispersive x-ray Spectroscopy (EDS), the compositions of the various iron-zinc phases within the coating were confirmed. A very thin layer of gamma (γ) phase, with zinc content in the range of 70-80%, is formed adjacent to the substrate steel. The thicker layer, with a light coloured, needle-like phase in a dark grey matrix, was confirmed to be a mixture of delta (δ) and zeta (ζ) iron-zinc phases, with the zinc content ranging from 90-95%. The outer layer on the chromated and non-chromated coating was confirmed to be the eta (η) phase, with zinc contents within the range of 96-100%. Due to its thinness (less than 1μm), the chromate layer was not detected with EDS. However, the presence of the chromate film was confirmed by its yellowish appearance compared to the bright silvery appearance of the non-chromated HDG bars. The weathered coating has a similar microstructure to both the non-chromated and chromated coatings; hence, it is not shown in Figure 4-1. The surface composition, however, was

confirmed by Raman spectroscopy (RS) to consist of zinc oxide and carbonate, as indicated in Figure 4-2.

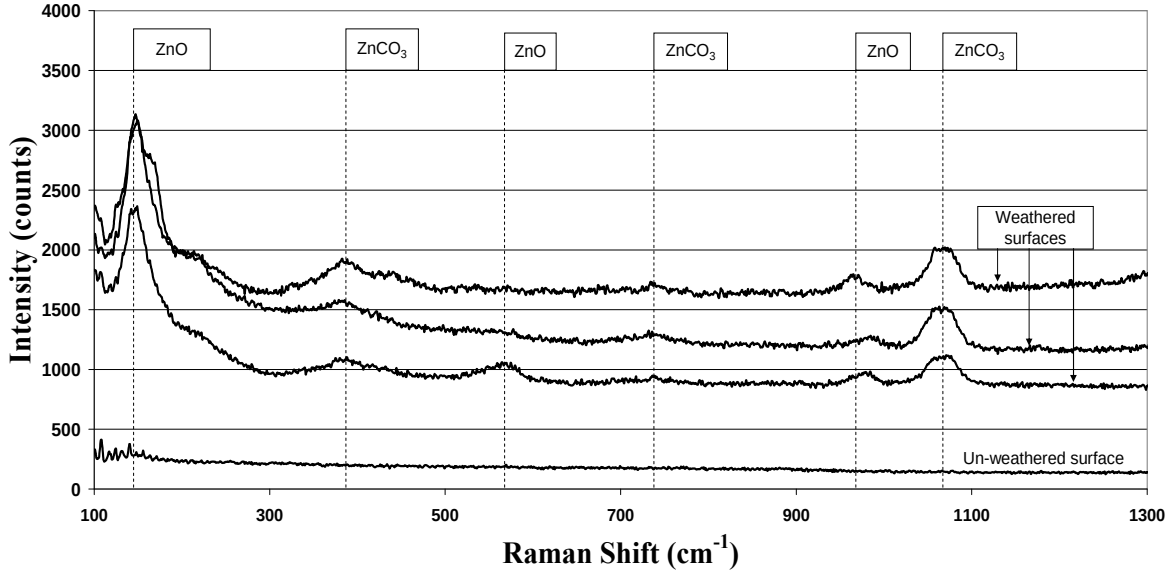

Figure 4-2. Raman spectra of weathered surfaces

4.2 Corrosion Results

4.2.1 Determination of Stern-Geary Constants

The Stern-Geary constant, B in Equation 3.2, was determined from cyclic polarization curves such as those shown in Figure 4-3 and Figure 4-4. The change in potential per decade of current for the cathodic Tafel line representing hydrogen evolution is illustrated in Figure 4-3. The anodic Tafel line was then calculated as the difference between the cathodic Tafel line and the measured net current:

$$i_a = i_{meas} - i_c \qquad \textbf{Equation 4.1}$$

Where i_{meas}, i_a, and i_c are the measured (net), anodic, and cathodic currents respectively. For passive corrosion, the cathodic Tafel region for oxygen reduction was determined from Figure 4-4 and the anodic Tafel slope calculated as above. The type of cathodic reactions occurring during active and

passive corrosion was confirmed by corrosion current and potential monitoring of the HDG bars, which will be discussed below in conjunction with other corrosion data.

Based on Equation 2.9, the B values for active and passive zinc corrosion were determined to be 39mV and 20mV, respectively.

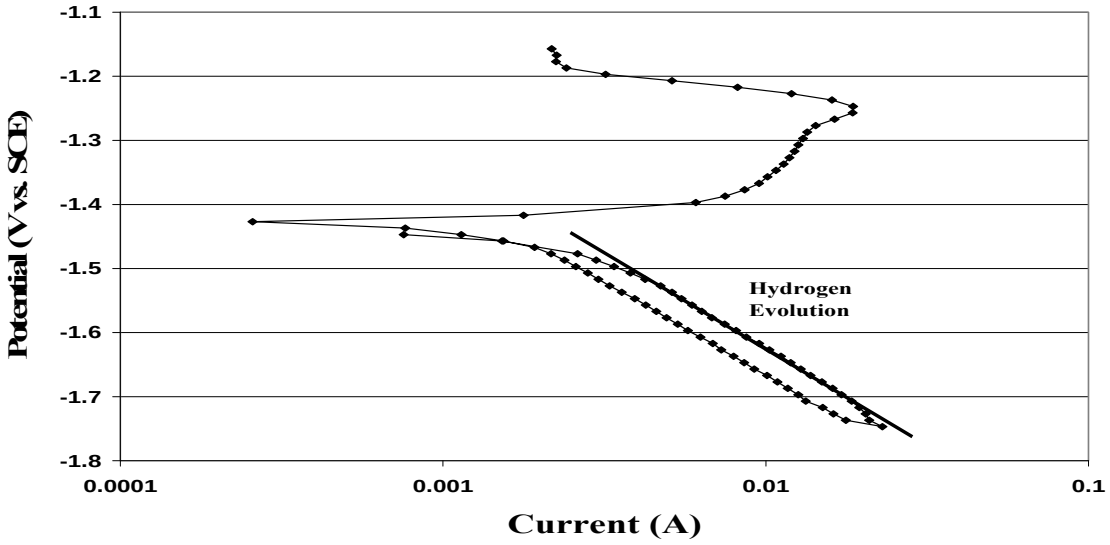

Figure 4-3. Cyclic polarization plot for active corrosion

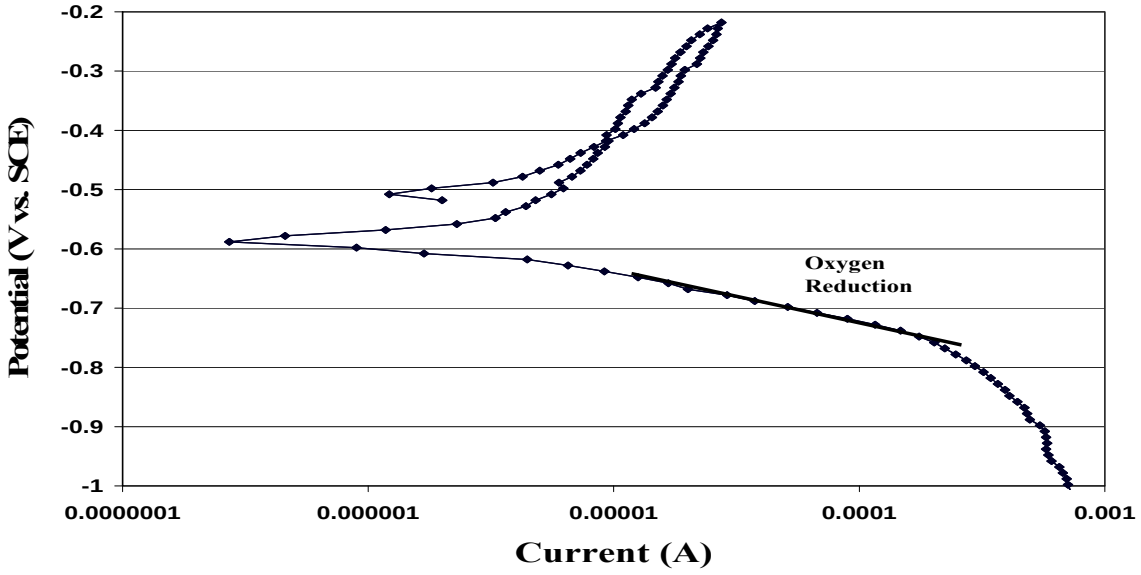

Figure 4-4. Cyclic polarization plot of passive corrosion

4.2.2 Corrosion Synthetic Pore Solution

The corrosion of HDG bars in solution is summarized in Figure 4-5 and Figure 4-6. It is confirmed that bars exposed to pH 13.3±0.1 and 13.7±0.1 did not passivate. However, it is evident that the chromate film increases the corrosion resistance under high pH. The annealed specimens also showed lower corrosion rates than the non-chromated, which is attributed to the lower zinc content on the surface.

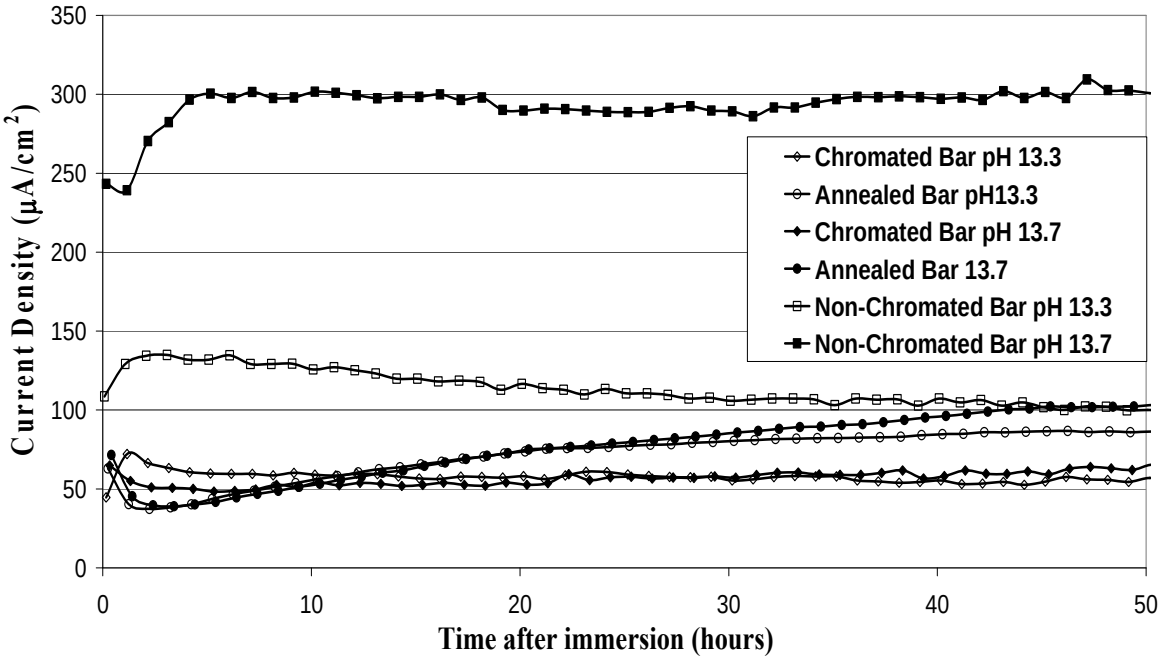

Figure 4-5. Corrosion of HDG bars when exposed to pH 13.3 and 13.7

When exposed to saturated $Ca(OH)_2$, passivation occurred for all types of HDG bars. Although the time required for passivation of the chromated and non-chromated bars is similar, the passive current density is slightly higher for the chromated specimens, indicating that the CHZ layer is more protective than the chromate film. For the annealed specimens, passivation required a longer time, again because less zinc is available on the surface. A second peak prior to passivation is apparent. Since only one specimen was monitored, conclusive comments cannot be made regarding this behaviour in solution; however, it is likely attributed to the lack of the pure zinc layer on the surface.

It can be seen from Figure 4-7 that CHZ crystal size increases with increasing pH, in agreement with the work of Andrade et al. [5]. Comparing the different HDG bars at pH 13.7±0.1, it is apparent from Figure 4-8, that the amount of CHZ is a function of the availability of zinc on the surface. The CHZ volume is the highest on the non-chromated bar and lowest on the chromated bar. Although the CHZ was not visible on the chromated bar, it was detected by Raman spectroscopy.

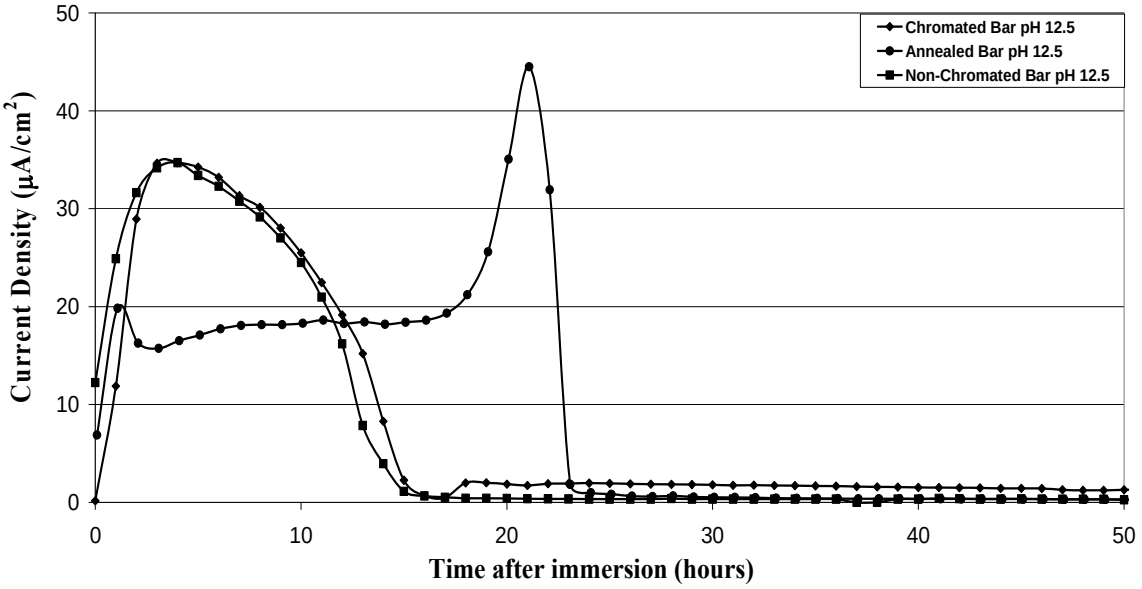

Figure 4-6. Corrosion of HDG bars when exposed to pH 12.5

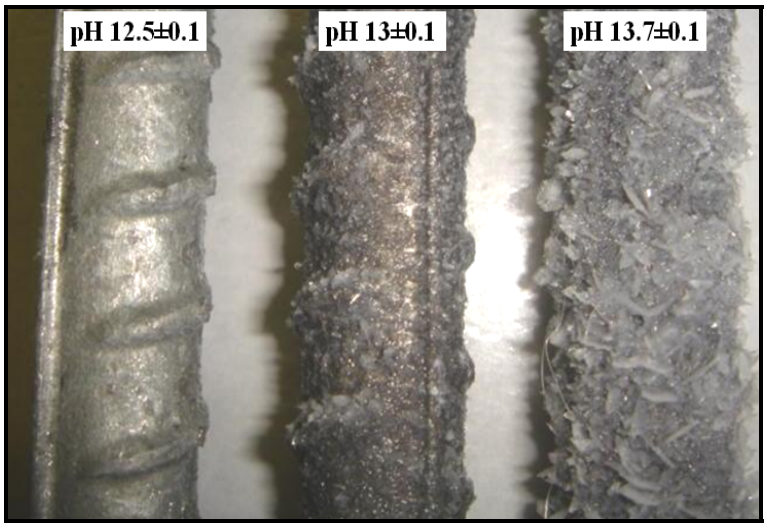

Figure 4-7. Increase in CHZ crystal size with respect to pH on non-chromated bars

Figure 4-8. CHZ formed on bars with different coatings in pH 13.7 (a) non-chromated, (b) annealed, and (c) chromated

4.2.3 Standardization of Calcium Hydroxyzincate

The x-ray diffraction pattern of the CHZ powder obtained from non-chromated bars exposed to pore solution of pH 13.7 is shown in Figure 4-9. Since it corresponds well with that for CHZ in the literature [38], the Raman spectrum of the same CHZ, shown in Figure 4-10 served subsequently as a standard for detecting CHZ formed on bars embedded in concrete.

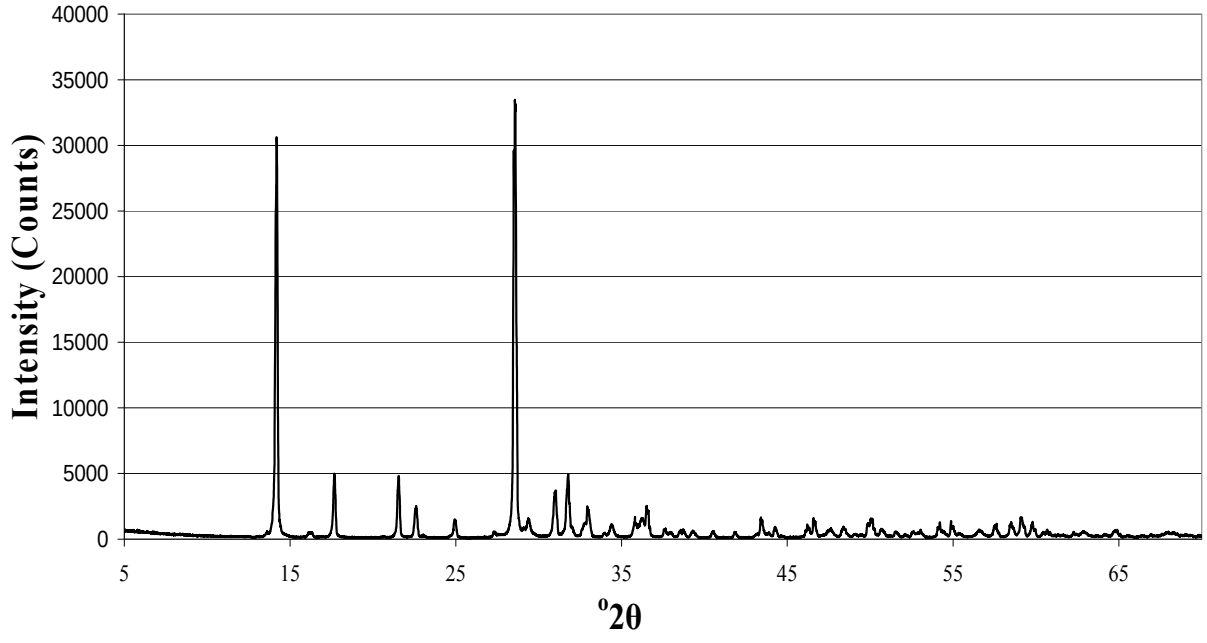

Figure 4-9. X-ray diffraction pattern of CHZ

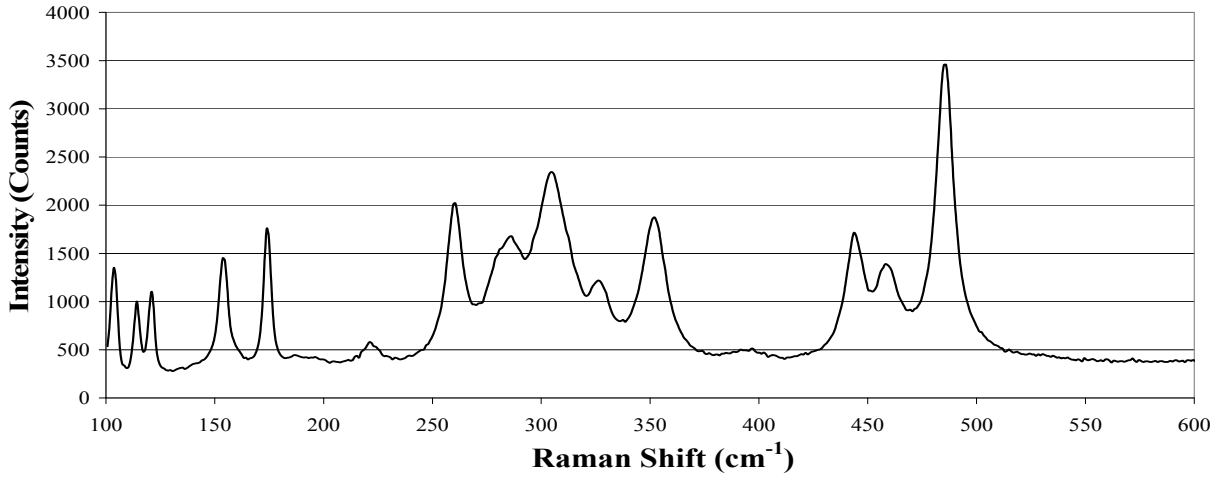

Figure 4-10. Raman spectrum of CHZ

4.2.4 Corrosion in Ordinary Portland Cement Concrete

The corrosion current and potential plots for the various HDG bars in the cylinders shown in Figure 3-1 are shown in Figure 4-11 through Figure 4-14 . The thick horizontal line represents the potential above which hydrogen evolution ceases and oxygen reduction occurs as the cathodic half cell reaction. From these results, it is clear that hydrogen evolution ceases when the bar becomes passivated. The characteristic of these plots will be further discussed in conjunction with the corrosion results presented below.

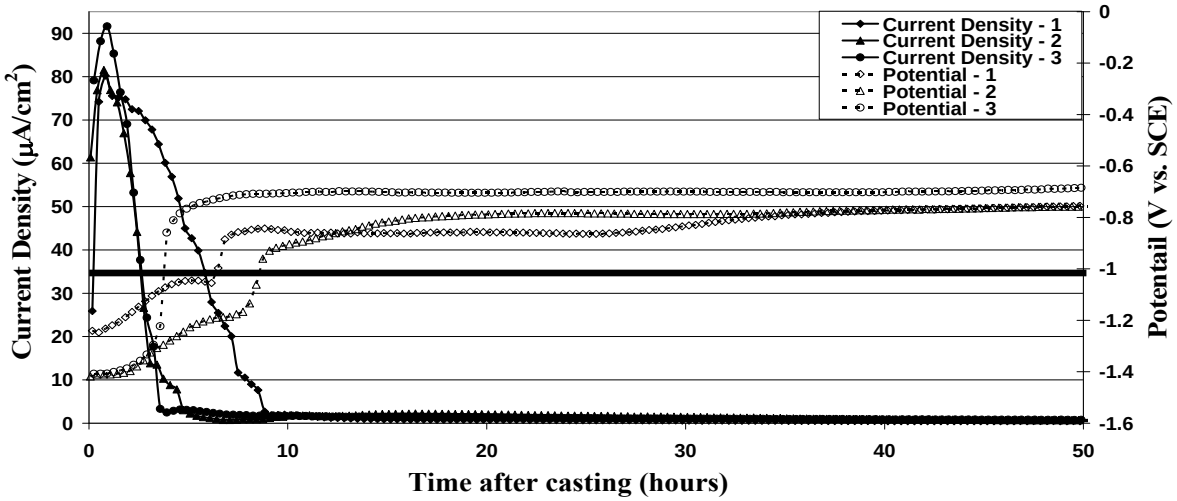

Figure 4-11. Corrosion current and corresponding half cell potential for three non-chromated bars

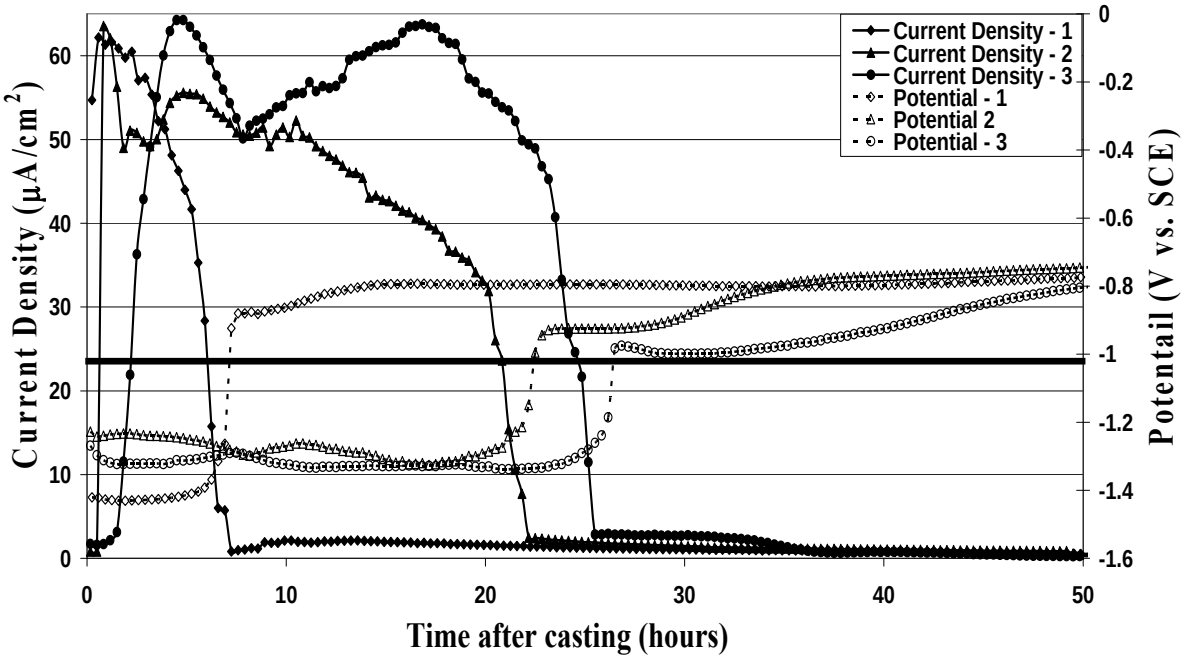

Figure 4-12. Corrosion current and corresponding half cell potentials for three chromated bars

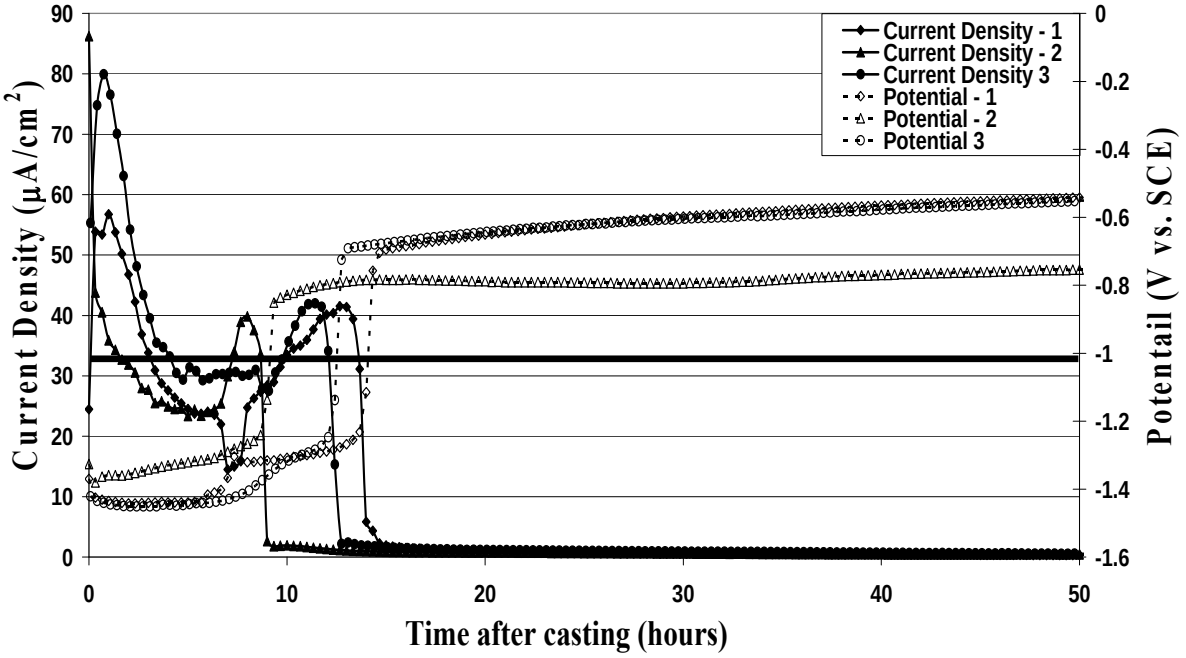

Figure 4-13. Corrosion current and corresponding half cell potential for three annealed bars

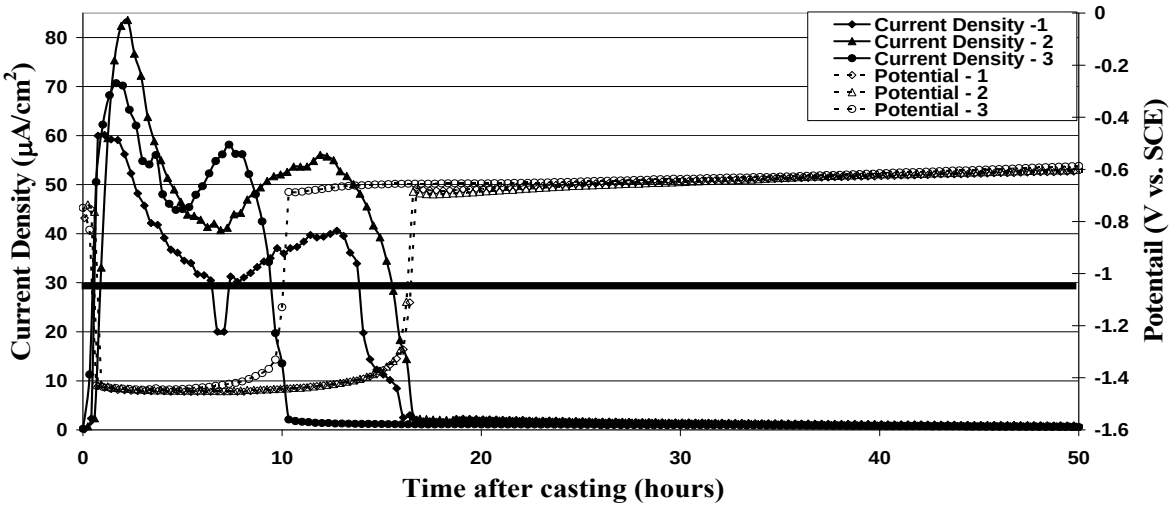

Figure 4-14. Corrosion current and corresponding half cell potential for three weathered bars

Corrosion results for HDG bars embedded in individual concrete cylinders illustrated in Figure 3-2b are shown in Figure 4-15. Only four specimens of chromated, non-chromated, and weathered bars are shown because of connection errors that led to unusable data for one specimen of each.

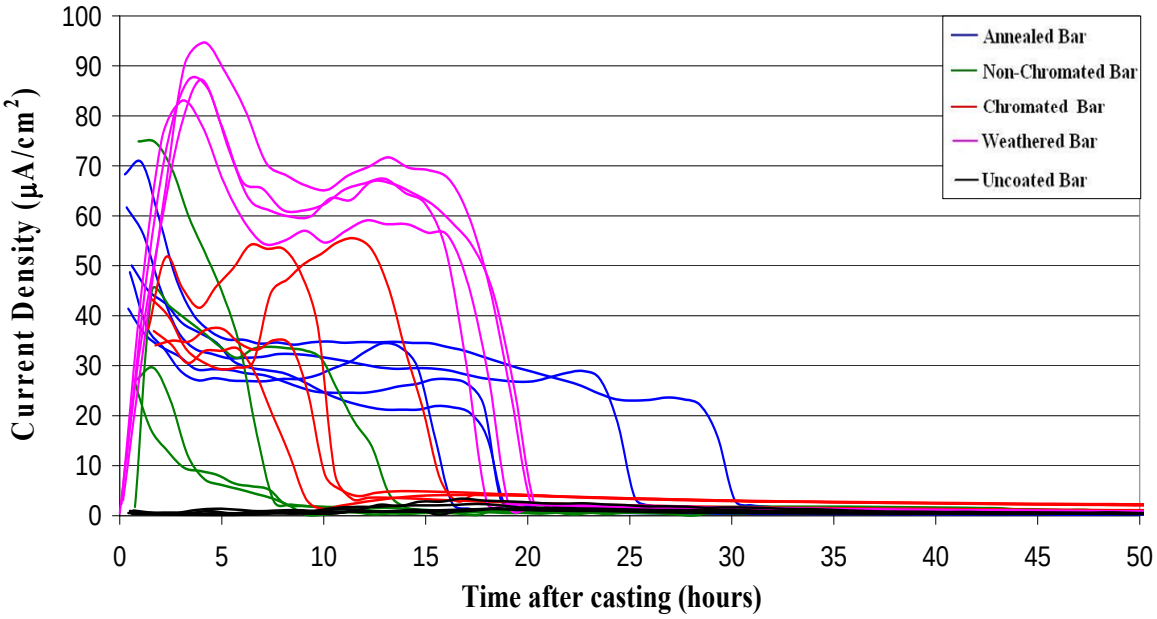

Figure 4-15. Corrosion of HDG bars in concrete

These data must be interpreted in light of the hydration of the cement, which is occurring simultaneously. Upon concrete mixing, the mixing water becomes saturated with Ca^{2+} and OH^- ions and also contains SO_4^{2-}, K^+, and Na^+ ions, causing a sudden increase in electrical conductivity and pH and, thereby, an initial increase in corrosion current. The subsequent decrease in corrosion rates can be attributed to a combination of (i) CHZ formation, (ii) lower ionic activity during the dormant period of cement hydration and (iii) a constriction of the initial mixing water into the developing pore structure of the cement paste. In this period, ettringite forms on unhydrated cement particles, temporarily preventing further release of ions into the pore fluid. At the end of this dormant period, osmotic pressure penetrates the ettringite coating and a rapid increase in hydration occurs, leading to an increase in ionic mobility. At this point, Ca^{2+} and OH^- ions reach a critical concentration allowing the zinc to passivate rapidly.

The weathered bars displayed significantly lower initial corrosion rates than the other bars. This is attributed to the existing layer of zinc oxide and zinc carbonate on the surface which protected the zinc. In concrete, this layer dissolved quickly, thereafter allowing the zinc to corrode. Prior to passivation, the delay in the onset of zinc corrosion led to higher corrosion rates than those observed for other HDG bars probably because of:

1. the shorter period of time in the wet cement for CHZ formation, and
2. the higher pH and ionic activity of the concrete pore fluid once the protective coating had dissolved.

A general trend in corrosion for the weathered and the chromated bars was observed. After the initial peak, corrosion decreased, possibly due to a combined effect of CHZ formation and the changes in ionic activity of the pore solution described above. Then the corrosion rate increased again, possibly due to the increased ionic activity in the pore solution at the end of the dormant period of hydration. The combined effect of concrete setting and CHZ formation then led to rapid passivation of the bars.

For most of the non-chromated specimens, the second corrosion peak was not observed. The higher availability of zinc at the surface may allow the passivation to occur sufficiently fast that the subsequent peak could be prevented. A second peak however was observed for one specimen. This deviation is assumed to be an effect of insufficient pure zinc on the surface of that particular specimen.

The annealed specimens, on the other hand, had a relatively stable corrosion current after their initial peaks. A slight increase in corrosion rate at the end of the dormant period could be attributed to the lack of pure zinc on the surface, which also explains the longer average passivation time.

As expected, the control specimens (labelled uncoated bars in Figure 4-15) remained passive, but a slight increase in current was observed at the end of the dormant period similar to HDG bars, which is believed to be an effect of ionic activity as discussed above.

The corrosion potentials and corrosion rates of specimens, illustrated in Figure 4-11 through Figure 4-14 displayed similar trends. The corrosion rates of the annealed specimens, shown in Figure 4-13, however showed more noticeable second peaks than those shown in Figure 4-15. This difference is probably a result of inconsistency in surface zinc content. These specimens were not actually annealed under controlled conditions but were more slowly cooled after the excess zinc had been removed by spinning and, thus, would not have identical or uniform surface layers. Consequently, specimens shown in Figure 4-13 may have had higher amounts of pure zinc on the surface leading to a higher corrosion current at the end of the dormant period.

4.2.5 Coating Depth Losses in OPC Concrete

The total depth loss of zinc for each specimen was calculated from the areas under the current versus time curves and their average is plotted with respect to time in Figure 4-16. Table 4-1 summarizes the corrosion data and average coating depth losses for the four types of bars.

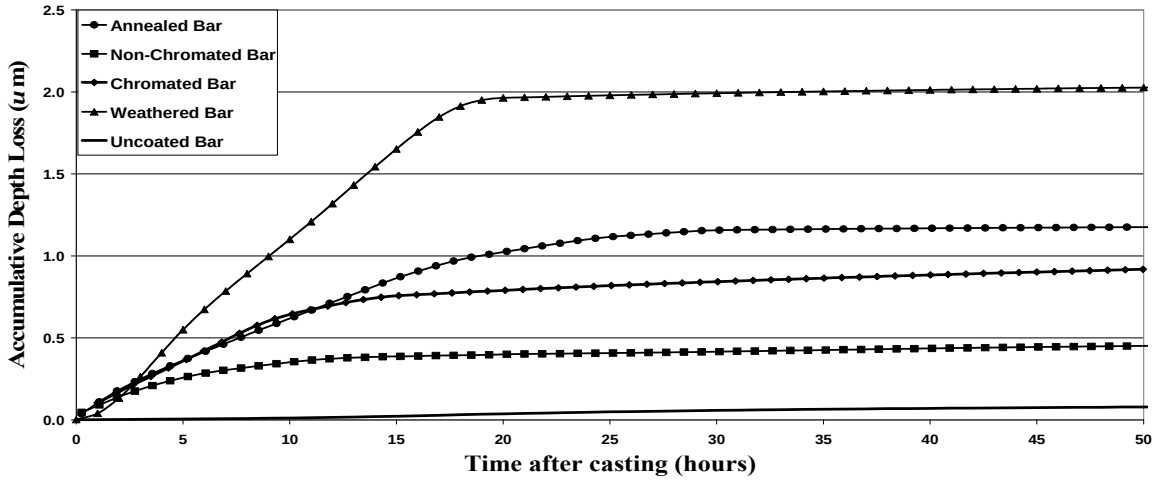

Figure 4-16. Cumulative depth loss in the first two days

Table 4-1. Corrosion current and depth loss summary in OPC concrete

Bar Type	Max. active i_{corr} ($\mu A/cm^2$)	Min. passive i_{corr} ($\mu A/cm^2$)	Average depth loss @ 50 hours (μm)
Weathered	83-95	0.6-0.8	2.03
Annealed	41-70	0.2-0.6	1.18
Chromated	37-55	1.1-2.3	0.92
Non-chromated	30-75	0.5-0.7	0.45
Control	1.3-3.4	0.3-0.5	0.07

With the typical coating thickness on HDG bars ranging between 100-350 μm, the depth losses are considered insignificant. An i_{corr} of 1 $\mu A/cm^2$ corresponds to 15 μm depth loss per year. As summarized in Table 4-1, i_{corr} in the passive state is lower than $1\mu A/cm^2$ for all non-chromated bars. By extending the corrosion monitoring of selected specimens up to four days, it was found that i_{corr} decreased to values that ranged from 0.1 to 0.3 $\mu A/cm^2$, similar to those reported in the literature for passive HDG steel [15, 35, 39]. From Table 4-1, it is clear that, in the passive state, the corrosion current density is slightly higher for chromated bars than for other HDG bars. This is reflected by the higher slope of the depth loss plot in Figure 4-16.

4.2.6 Corrosion in Silica Fume and Slag Concrete

Corrosion of chromated and non-chromated HDG bars in silica fume and in slag concrete, as summarized in Figure 4-17 and Figure 4-18, displayed significantly different corrosion behaviours from those observed in OPC concrete.

The initial corrosion current densities are, on average, higher than those measured in OPC concrete. Also different from those in OPC concrete, in silica fume concrete a second peak in corrosion current is apparent for the non-chromated bars. In both silica fume and slag concrete, the bars did not achieve passivation within the initial two days: their corrosion current densities were much higher than $1\mu A/cm^2$. These characteristics are attributed to the effect of faster pH development in silica fume and slag concrete than in OPC concrete.

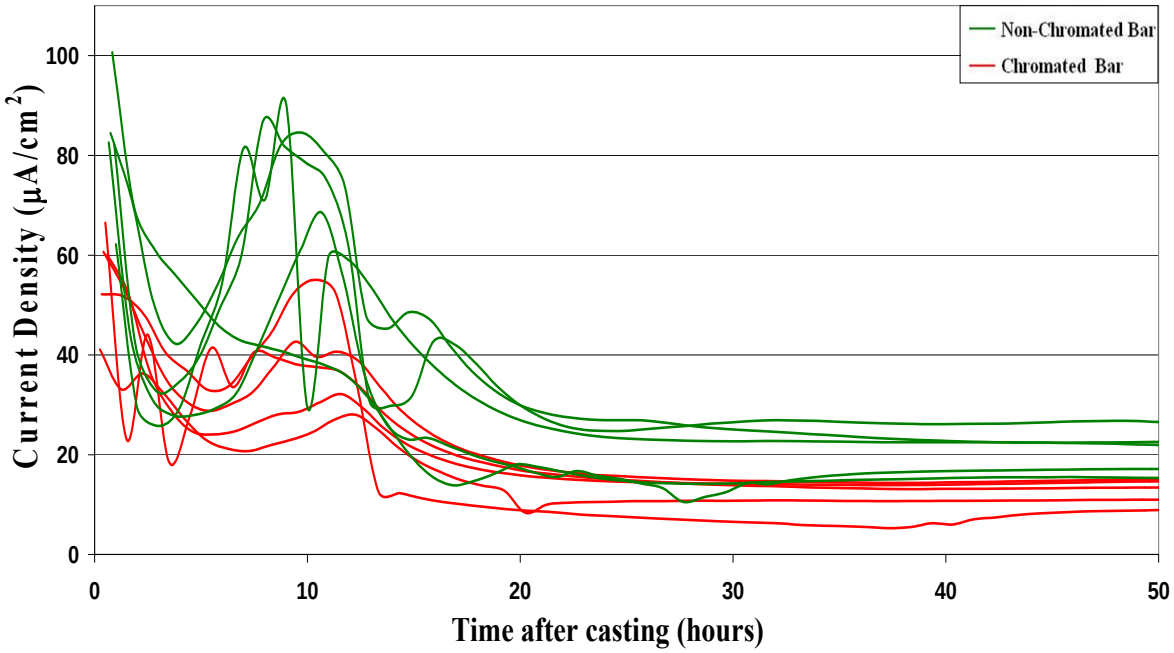

Figure 4-17. Corrosion of chromated and non-chromated bars in silica fume concrete

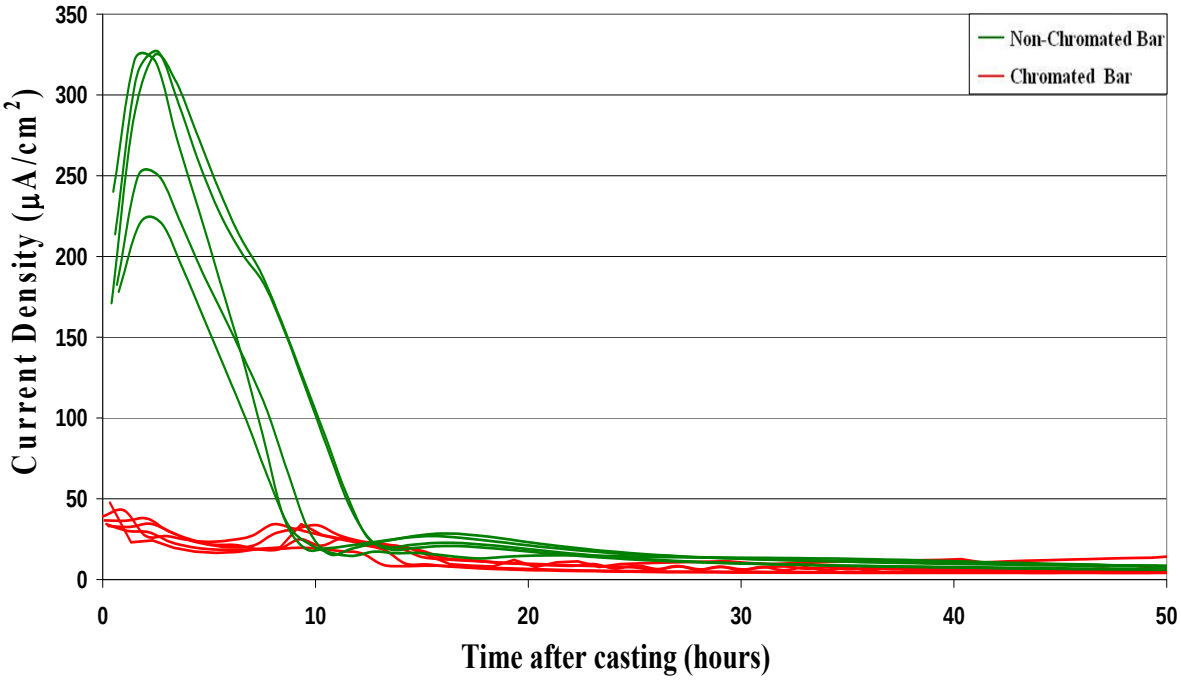

Figure 4-18. Corrosion of chromated and non-chromated bars in slag concrete

By comparing the pH development for the different concretes, Figure 4-19 through Figure 4-21, it is evident that the initial pH and its rate of increase for both the silica fume and slag concrete was higher, on average, than for OPC concrete. From the temperature profile of the silica fume and slag concrete, it appears that the minor peaks and troughs in pH related to the temperature change. The pH values determined from titration of extracted concrete pore fluid at selected times indicate that the pH values measured in situ by the Ir/IrO_2 electrodes are slightly higher. The in situ monitoring indicates a major drop in pH at approximately 8 hours. However, the cause for this phenomenon is currently not known and further investigation is required. Aside from the discrepancies in pH values measured by the two methods, they both indicate higher initial pH and faster development for both the silica fume and slag concrete than for OPC concrete.

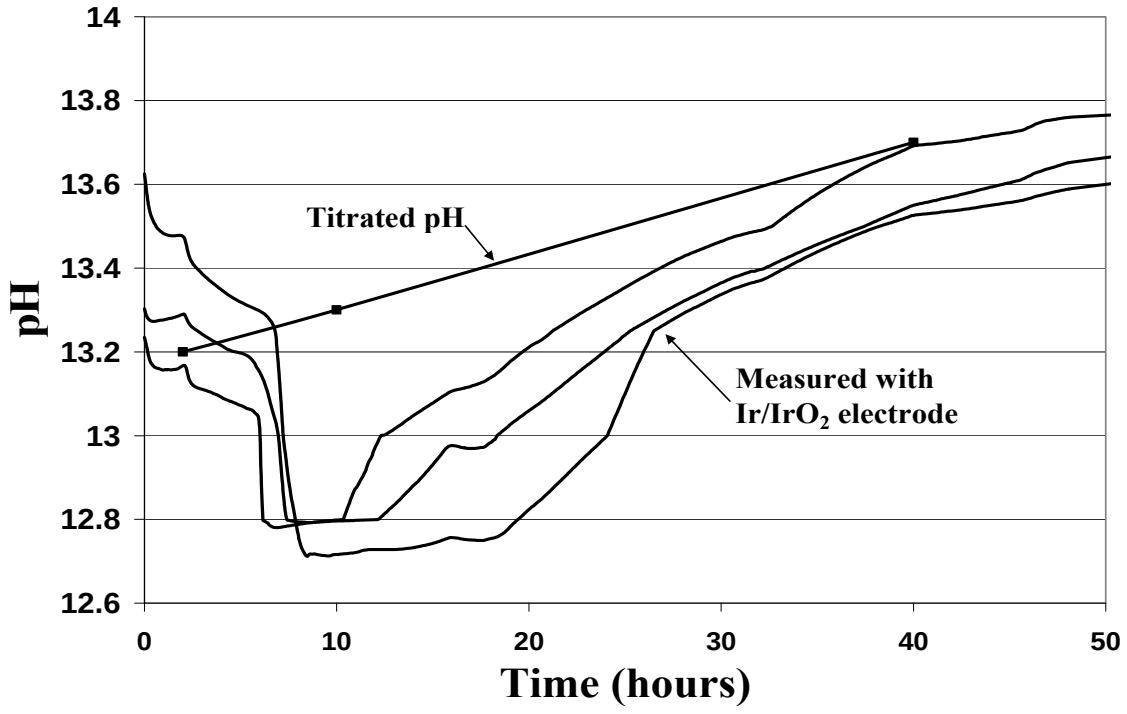

Figure 4-19. pH profile of OPC concrete

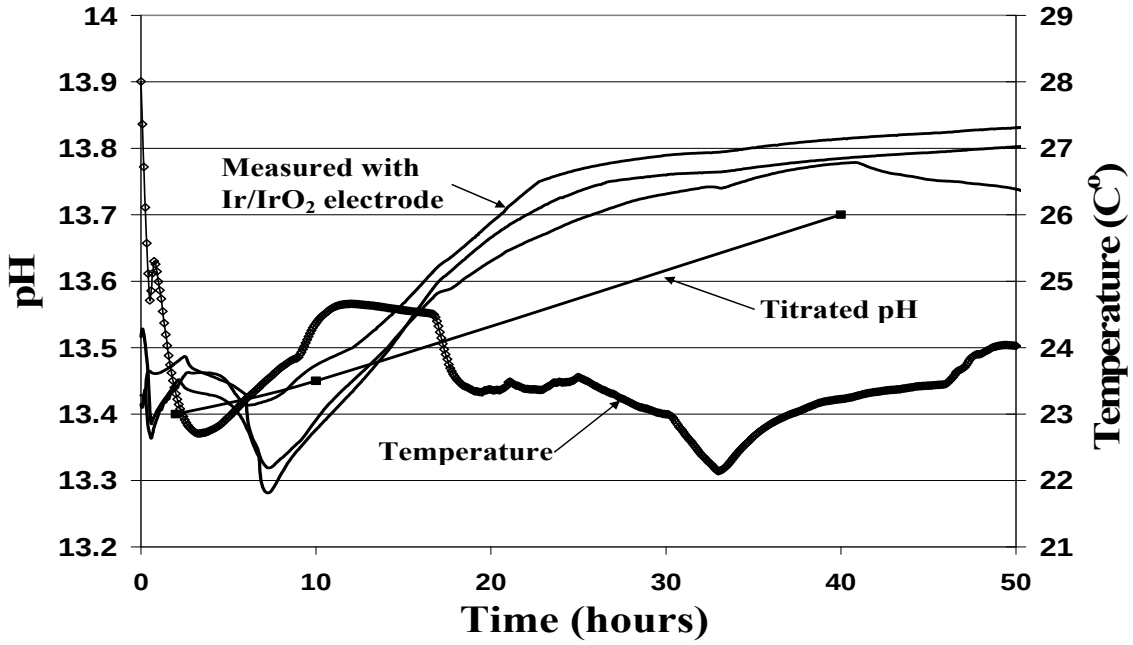

Figure 4-20. pH and temperature profile of silica fume concrete

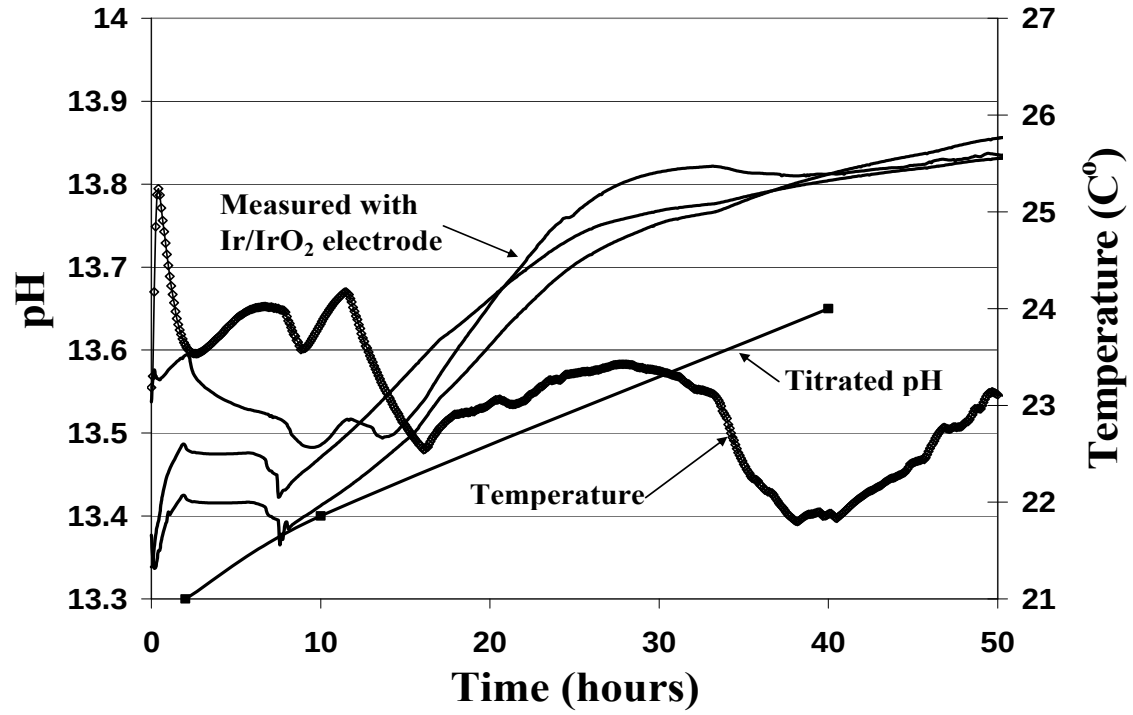

Figure 4-21. pH and temperature profile of slag concrete

With higher pH in silica fume concrete, the non-chromated specimens were not able to passivate at the same rate as those in OPC concrete; hence, the second corrosion peak occurred after the dormant period.

In slag concrete, the pH is slightly lower than that in silica fume concrete. It is believed that at this lower pH, the CHZ layer formed provided sufficient protection to the zinc, preventing the second corrosion peak from occurring. This behaviour was not observed for chromated bars because the chromate film retarded the formation of CHZ.

From the corrosion data presented here it is clear that under non-passivating conditions, such as those during the early hydration of silica fume and slag concrete, chromate treatment improves the resistance to corrosion for HDG bars.

Despite the similarity in pH between silica fume and slag concrete, the initial corrosion peaks for non-chromated bars in slag concrete are significantly higher than those observed in silica fume concrete. A possible cause for this phenomenon is the slower reactivity of slag particles compared to silica fume particles. Therefore, for cement containing slag, during the first several hours, more mixing water is available for hydration of the ordinary Portland cement component of the blended cement. This increases the water to binder ratio which gives rise to highly porous concrete during this initial stage of hydration, consequently, allowing high ionic mobility through the concrete and, thus, higher corrosion current.

Since passivation was not observed in the initial two days, the corrosion in both the silica fume and slag concrete specimens was monitored beyond two days in order to assess the corrosion behaviour over time.

For bars in silica fume concrete, the corrosion was monitored at selected times, up to a period of one month. As shown in Figure 4-22, corrosion rates gradually decreased over time; however, at the end of one month, corrosion remained active with current densities higher than $1\mu A/cm^2$. Nevertheless, based on the decreasing trend, it is reasonable to assume that over time, passivation would occur.

A close examination of the current densities at the end of the one month period revealed that non-chromated bars reached slightly lower corrosion rates on average than the chromated bars. This further confirms that chromate treatment is not necessary.

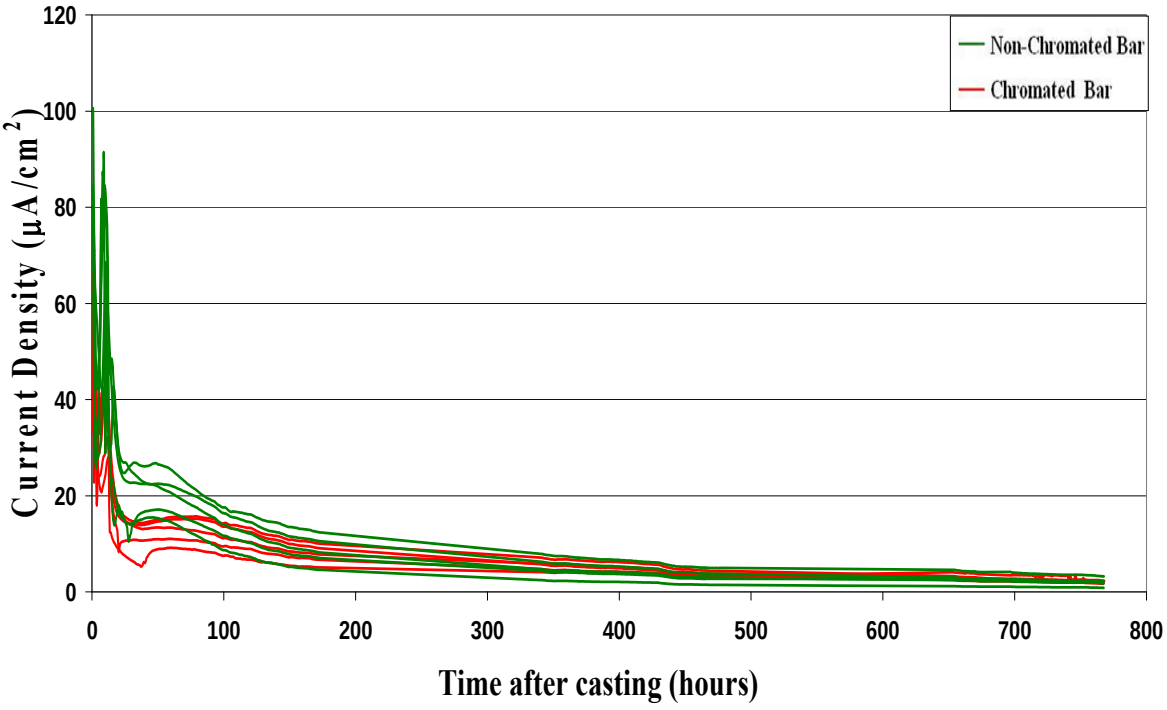

Figure 4-22. Extended corrosion monitoring in silica fume concrete

For the slag concrete specimens, corrosion was monitored for approximately eighteen days. After four days, the corrosion of the non-chromated bars reached a passive state, suggesting that the level of protection provided by CHZ in concrete may differ from that in solutions. Despite high pH (>13.3), due to the confinement at the concrete and steel interface, a passive layer of CHZ can form. In slag concrete, this phenomenon occurred sooner than in silica fume concrete possibly because the pH is slightly lower, allowing more protective CHZ to be formed.

Chromated bars in both silica fume and slag concrete exhibited an increase in corrosion at approximately two days as shown in Figure 4-22 and Figure 4-23. In silica fume concrete, the non-chromated bars also displayed this behaviour. An examination of the corrosion for non-chromated and annealed bars in OPC concrete, Figure 4-24, which had been monitored beyond two days indicates that such behaviour does not exist. Therefore, the increase in corrosion beyond two days is likely an effect of silica fume and slag reactivity, which increases the alkali content and ionic activity of the concrete pore fluid. For the non-chromated bars in slag concrete, since sufficient passivation was achieved, the increase in corrosion was prevented.

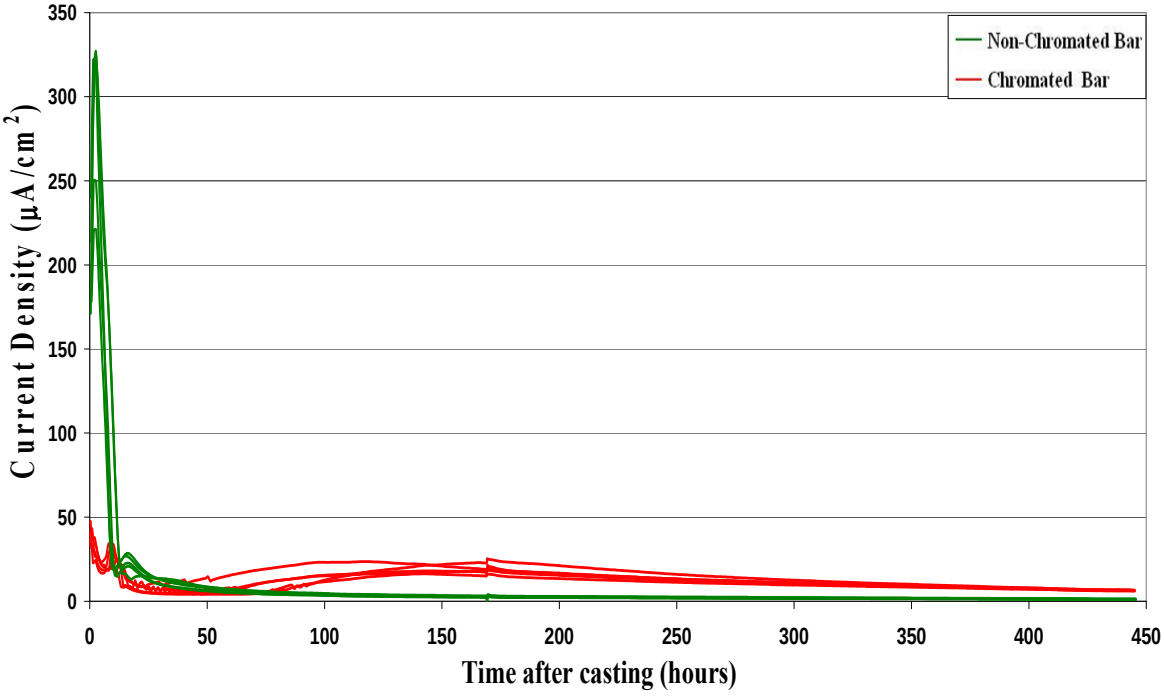

Figure 4-23. Extended corrosion monitoring in slag concrete

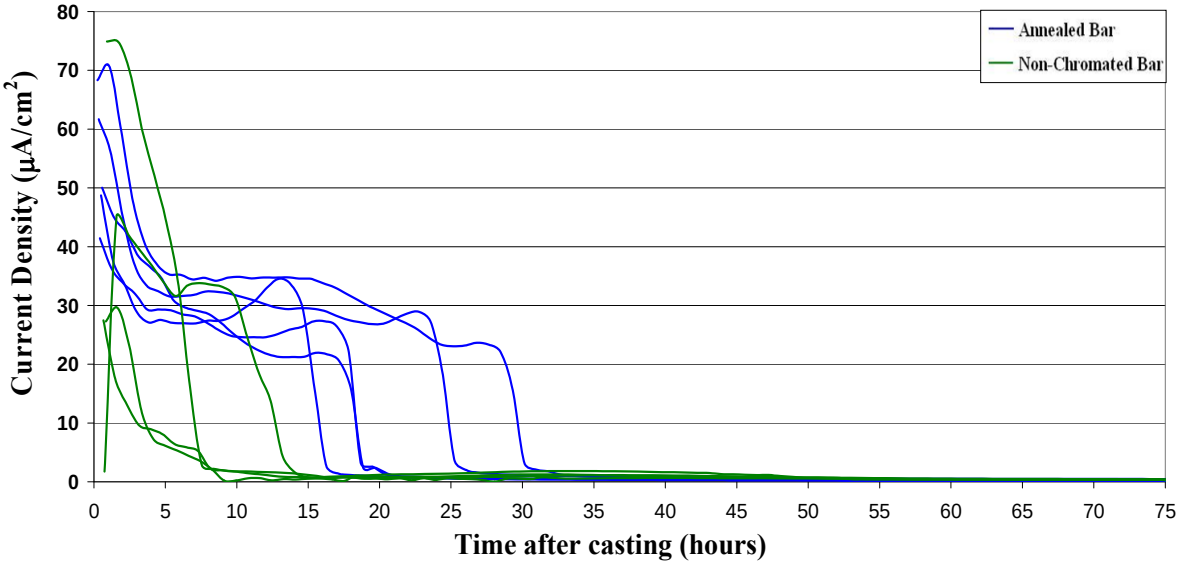

Figure 4-24. Extended corrosion monitoring of non-chromated and annealed bars in OPC concrete

The coating depth losses over the initial two days and the extended monitoring period, as shown in Figure 4-25 through Figure 4-28, demonstrate the significance of the higher corrosion rates presented above.

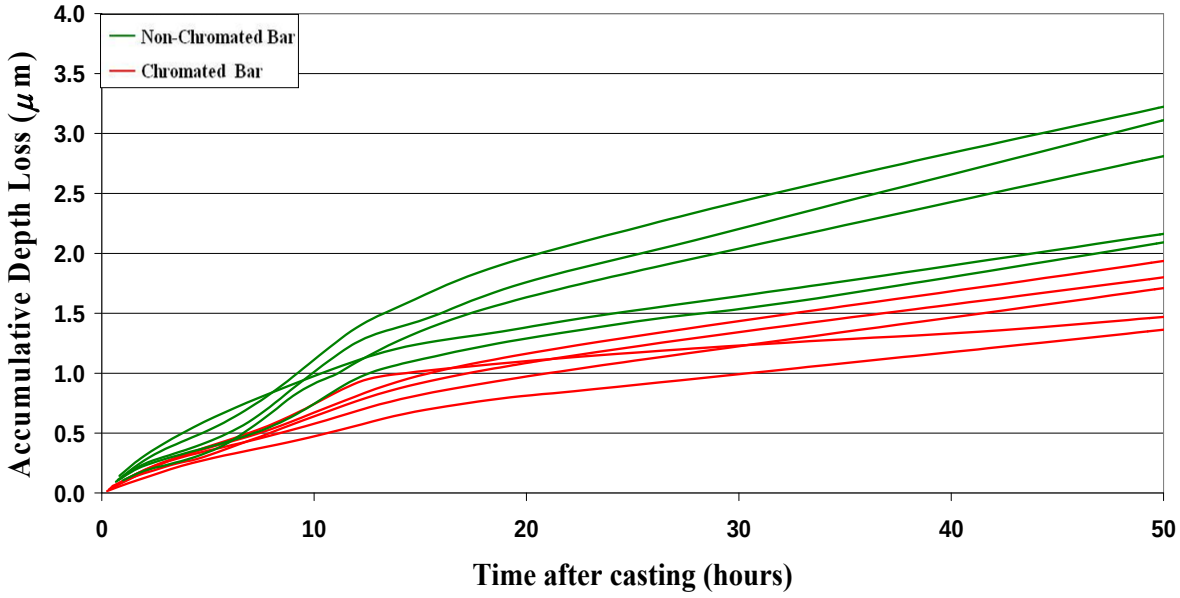

Figure 4-25. Coating depth loss in silica fume concrete over the initial two days

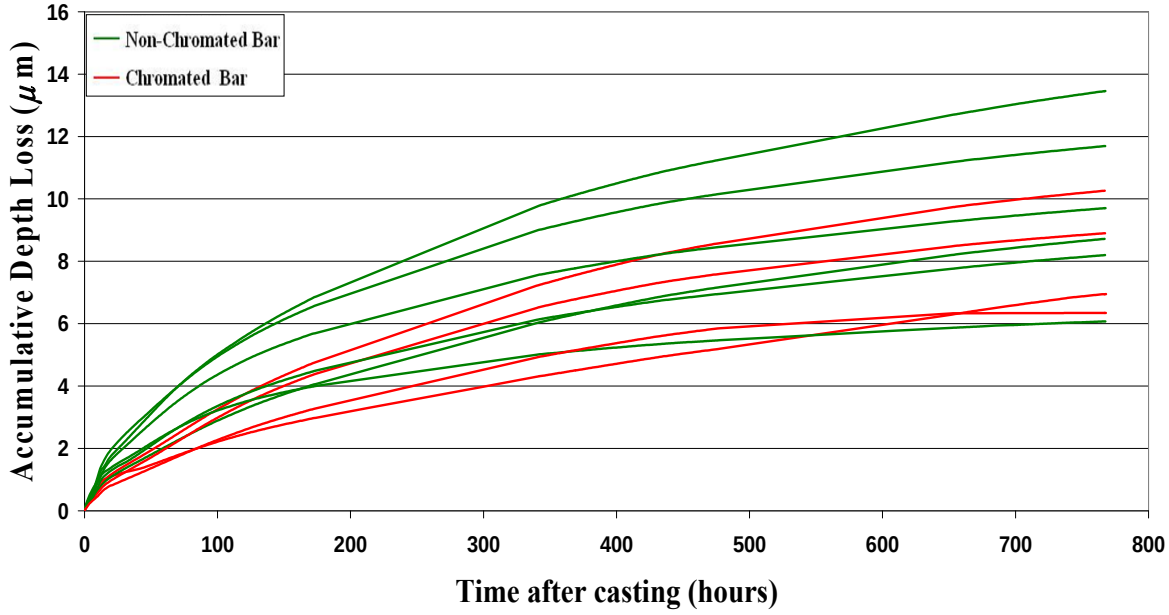

Figure 4-26. Coating depth loss in silica fume concrete over the initial month

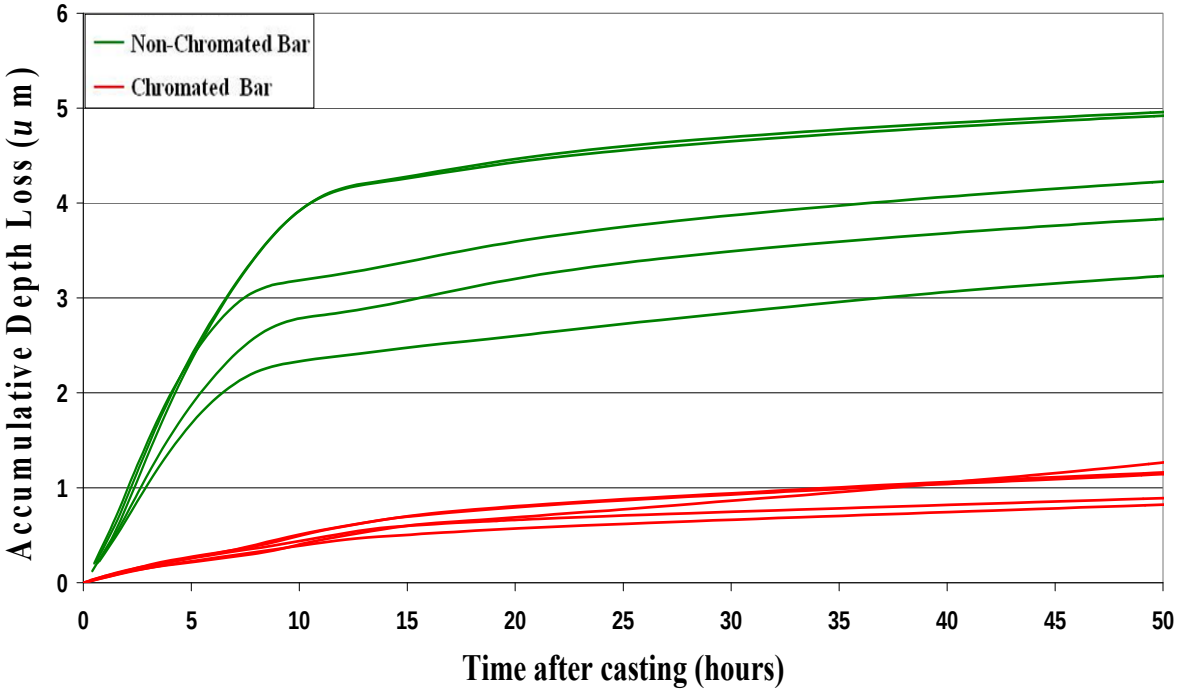

Figure 4-27. Coating depth loss over the initial two days in slag concrete

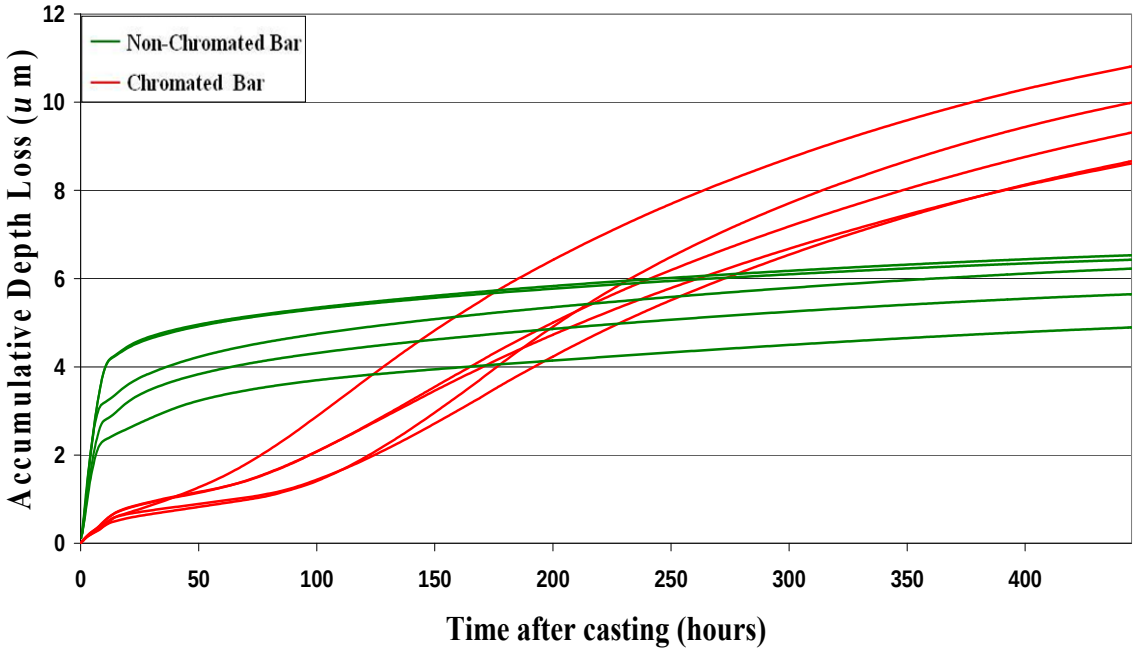

Figure 4-28. Coating depth loss in slag concrete over the initial eighteen days

Table 4-2 below summarizes the corrosion and depth loss for all bars in the three types of concrete used. Due to higher corrosion rates in silica fume concrete, the average coating depth losses for non-chromated and chromated bars were 6.5 and 2.4 times higher than those in OPC concrete for the initial two days. Over the span of one month, both the chromated and non-chromated bars lost significant amounts of their coating in silica fume concrete. From the slopes of depth loss plots, it is clear that passivation has not occurred and corrosion continues at a relatively high rate.

In slag concrete, the high corrosion rates for non-chromated bars led to depth losses that are on average, about 11 times higher than those in OPC concrete for the initial two days. However, with corrosion currents as low as 1.1 $\mu m/cm^2$ at the end of the monitoring period, the corrosion state is more or less considered passive, and it is reflected by the low slope of the depth loss plots. At the end of the eighteen day monitoring period, the total average depth loss is significantly less than that in silica fume concrete.

For the chromated bars in slag concrete, the increase in corrosion after two days led to depth losses comparable to those for silica fume concrete. Being in the active corrosion state, depth loss continues at a high rate as indicated by the high slop of the depth loss plot.

Table 4-2. Corrosion current and depth loss summary of all bar types in different concretes

	Specimen	Max. i ($\mu A/cm^2$)	Min. i ($\mu A/cm^2$)		Average Depth Loss (μm)	
			@ 2 Days	Extended	@ 2 Days	Extended
OPC	Black Bars	1.4-3.4	0.09-0.2	-	0.09	-
	Non-Chromated Bars	20-50	0.7-1.0	-	0.4	-
	Annealed Bars	28-48	0.6-1.2	-	0.8	-
	Weathered Bars	55-63	0.3-0.4	-	1.4	-
	Chromated Bars	25-38	1.5-3.0	-	0.7	-
Silica Fume	Non-Chromated Bars	60-90	15.4-26.7	0.9-3.2 @ 32 days	2.6	9.8 @ 32 days
	Chromated Bars	30-50	8.8-15.0	1.7-3.6 @ 32 days	1.7	6.9 @ 32 days
Slag	Non-Chromated Bars	220-330	6.3-8.8	1.1-1.3 @ 20 days	4.2	5.9 @ 20 days
	Chromated Bars	20-35	4.1-13.4	6.2-6.7 @ 20 days	1.0	9.5 @ 20 days

4.2.7 Resistance Development of Concrete

The development of electrical resistance for the three concrete types is plotted against time in Figure 4-29. As expected, the rate resistance increase of silica fume concrete was the highest compared to both slag and OPC concrete. The trends of resistance observed seem to correlate to neither the corrosion nor the pH as had initially anticipated. Therefore, the major changes in corrosion current and pH presented above were not due to changes in concrete resistance.

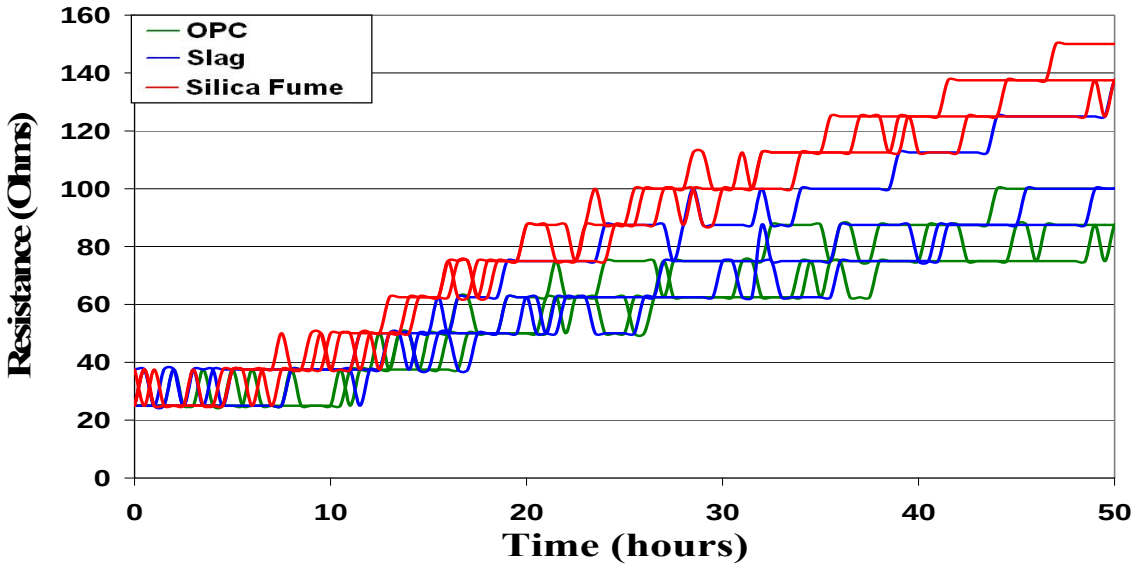

Figure 4-29. Resistance development of OPC concrete

4.3 Autopsy of Corroded Bars

4.3.1 Comparison of Surface Appearance of Corroded Bars

The degree of corrosion on bars after being embedded in concrete is reflected by the appearance of their surface. The darker the corroded surface, the higher the degree of corrosion. However, amongst the different types of bars exposed to OPC concrete, differentiation between their corroded surface appearances was difficult due to the similarity of their corrosion rates and the time taken to achieve passivation. Since the bars in OPC concrete passivated quickly compared to those in silica fume and slag concrete, the surface of the corroded bar remained relatively bright as shown in Figure 4-30. Due to higher corrosion rates and lack of passivity, the bars exposed to both silica fume

and slag concrete appeared significantly darker than those exposed to OPC concrete, as shown in Figure 4-31 and Figure 4-32.

Figure 4-30. Photograph of corroded bar exposed to OPC concrete

Figure 4-31. Photograph of corroded bar exposed silica fume concrete

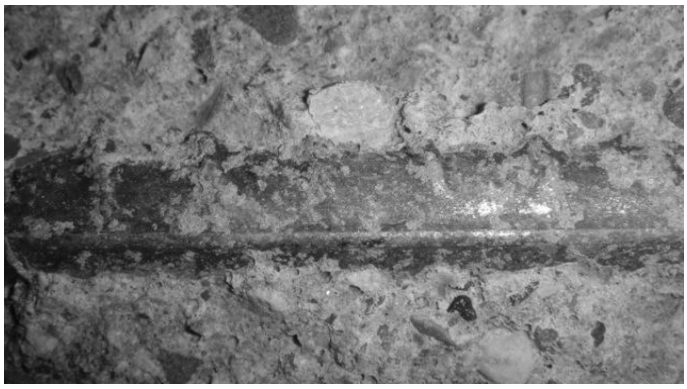

Figure 4-32. Photograph of corroded bar exposed to slag concrete

4.3.2 Identification of CHZ on Bars Exposed to Concrete

Through in-situ Raman analysis, the presence of CHZ on HDG bars exposed to OPC concrete was confirmed. Figure 4-33 illustrates typical spectra obtained for the various types of bars. The lower peak intensities, compared to the standard spectrum indicate lower concentrations of CHZ on bars exposed to concrete, compared to that formed in solution. This was expected because most of the CHZ was found to be incorporated into the adjacent cement. By analyzing numerous (10-15) locations on the surface of the bar and the cement adjacent to the bar, it was found that the frequency of detecting CHZ on chromated bars was generally lower than that on non-chromated HDG bars, further confirming that the chromate film retards CHZ formation.

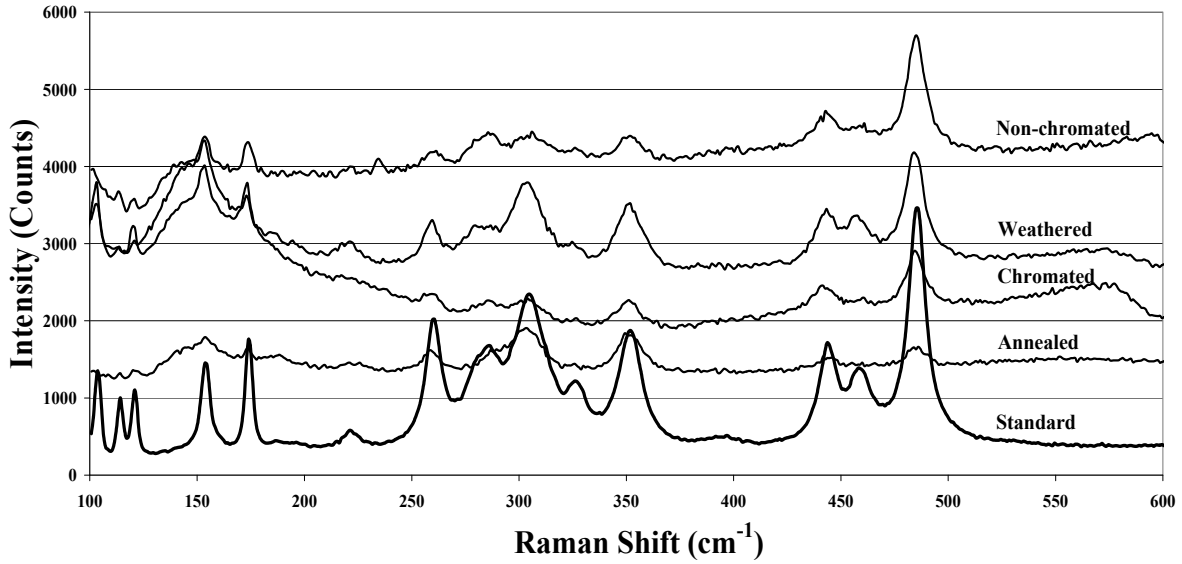

Figure 4-33. Spectra of CHZ on HDG bars exposed to OPC concrete

For both the silica fume and slag concrete specimens, Figure 4-34 and Figure 4-35, detection of CHZ was more difficult. This may be attributed to two factors:

1. fluorescence, as indicated by the high background of the spectra, may have masked out the CHZ peaks
2. less CHZ was formed on bars in these concretes due to higher pH which caused the calcium content of their pore fluid to decrease faster [31]

The latter is confirmed by more frequent occurrence of large peaks for zinc oxide at approximately 150cm^{-1}, which indicates that they did not undergo transformation to CHZ.

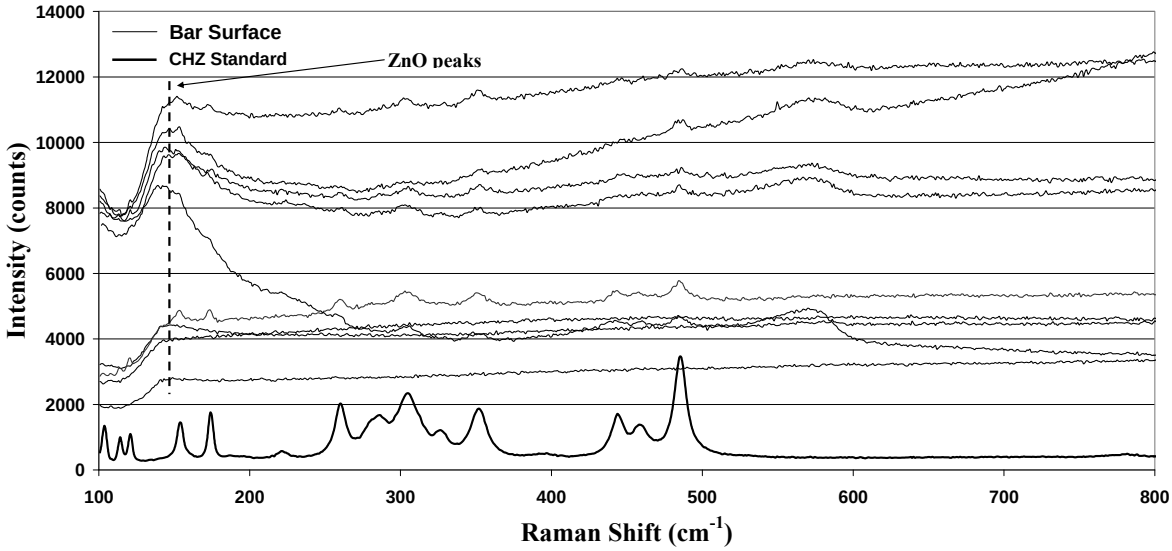

Figure 4-34. Raman spectra of chromated bars exposed to silica fume concrete

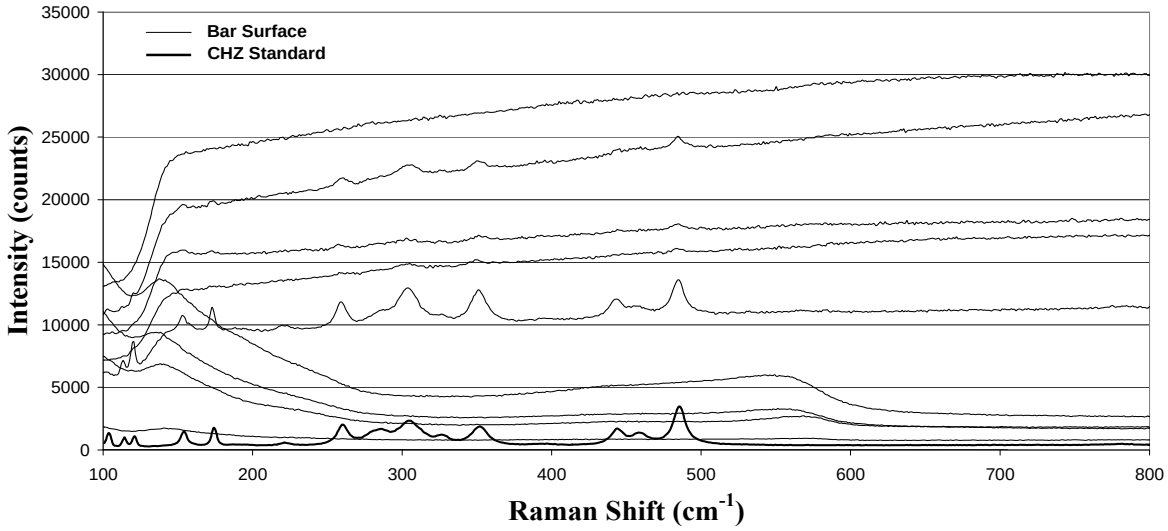

Figure 4-35. Raman spectra of chromated bars exposed to slag concrete

For the non-chromated bars in silica fume and slag concrete, Figure 4-36 and Figure 4-37, peaks for zinc oxides were also present. However, they are more pronounced for bars exposed to slag concrete because of their higher initial corrosion rates. The frequency of detecting CHZ on non-chromated bars was significantly higher than on the chromated bars because of the higher availability of zinc at the surface.

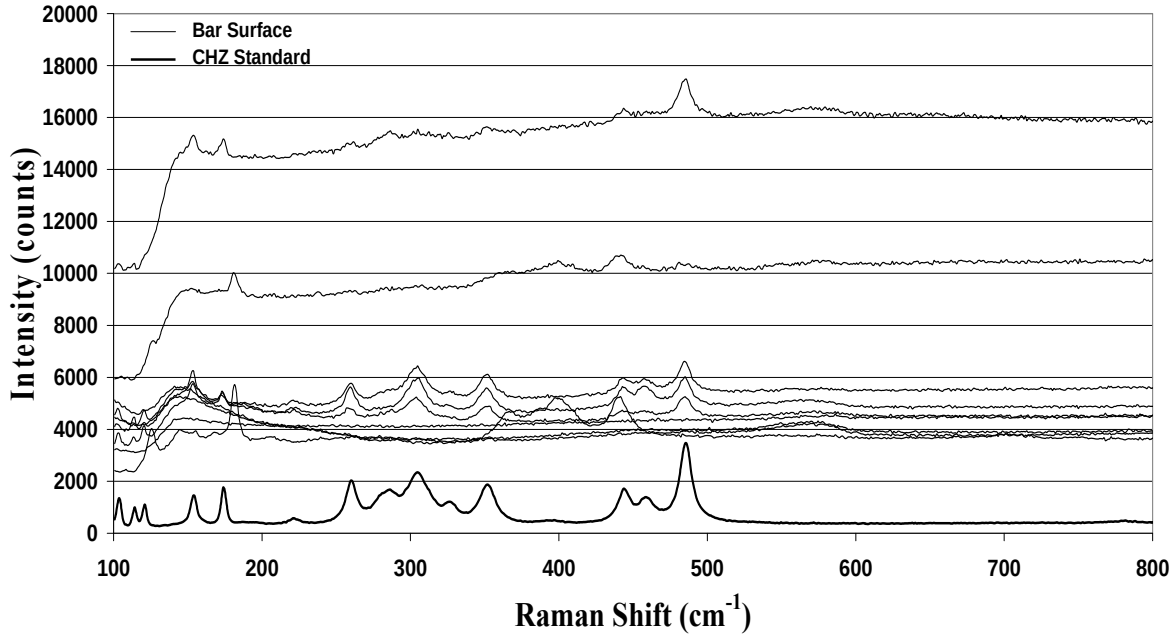

Figure 4-36. Raman spectra of non-chromated bars exposed to silica fume concrete

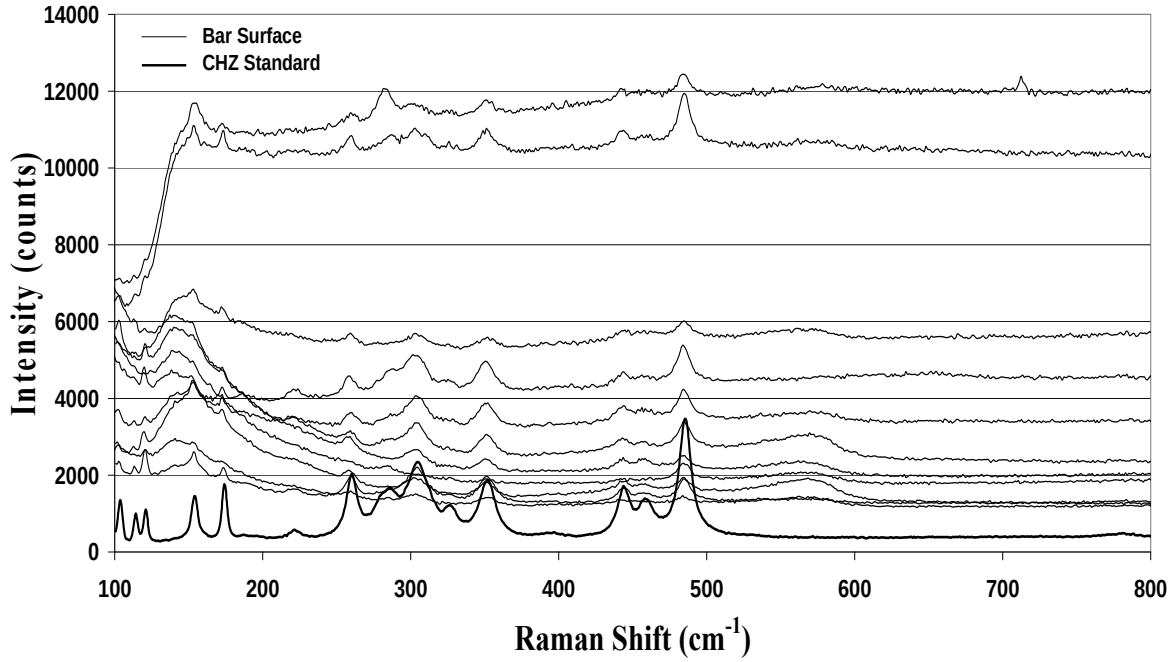

Figure 4-37. Raman spectra of non-chromated bars exposed to slag concrete

4.4 Mercury Intrusion Porosimetry

From the plots of pore radius, in micrometres, versus the cumulative intrusion volume, in cubic millimetres per gram of cement, it is evident that there is a discrepancy in pore size distribution between the OPC cement adjacent to uncoated bars when compared to that adjacent to HDG bars. For the uncoated specimens, a discontinuity in their pore size distribution is apparent in Figure 4-38. A possible cause of this phenomenon could be the layer of calcium hydroxide that is typically deposited at bar/cement interface, blocking some of the larger pores. For specimens adjacent to HDG bars, this layer of calcium hydroxide may not exist or exist at a lower quantity as it would have been consumed during the formation of CHZ. For both the silica fume and slag cements, a similar but less pronounced discontinuity was also observed, likely because less CHZ was formed in these cements compared to OPC cement and, therefore, less of the calcium hydroxide layer was consumed.

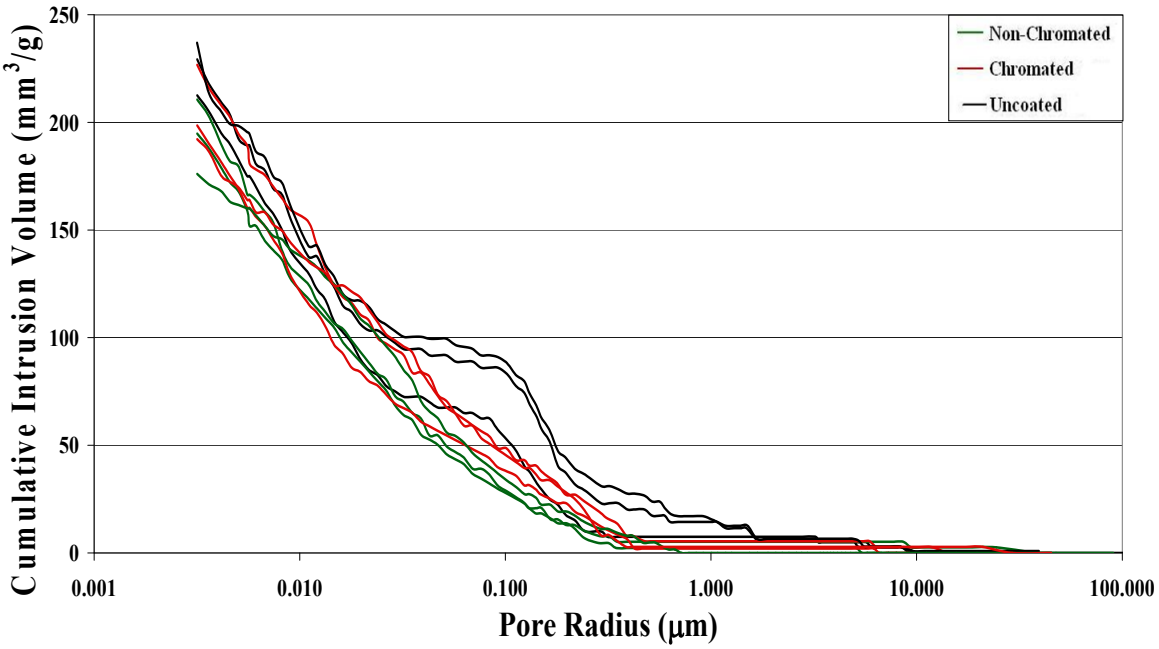

Figure 4-38. Pore size distribution of OPC cement adjacent to HDG and uncoated bars

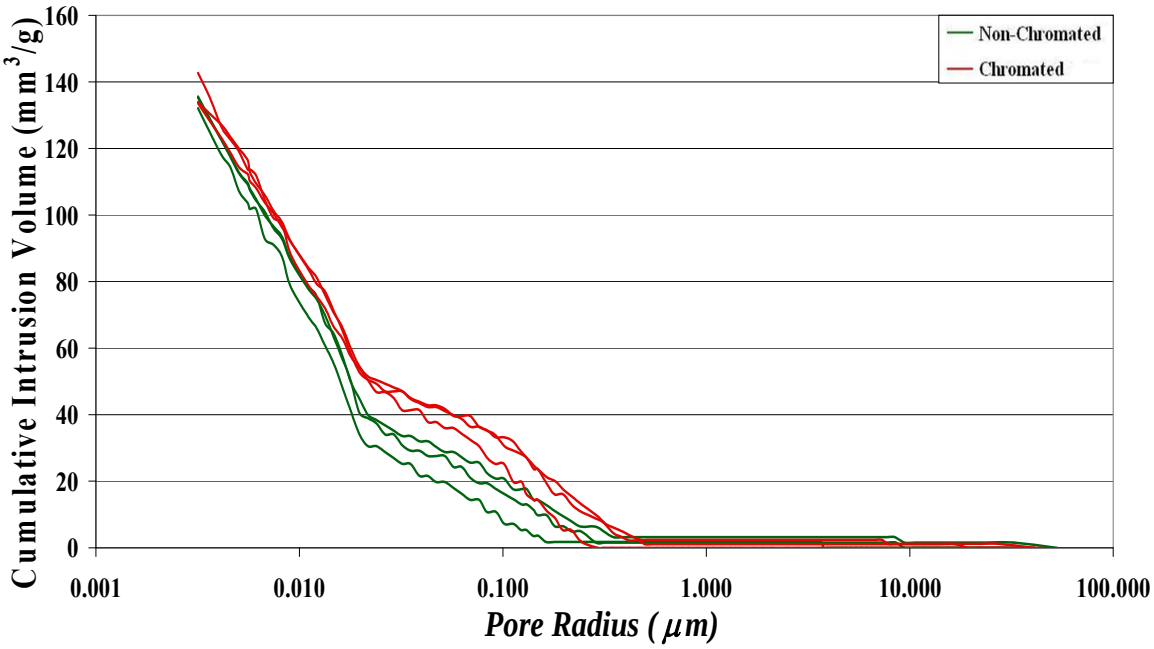

Figure 4-39. Pore size distribution of silica fume cement adjacent to HDG bars

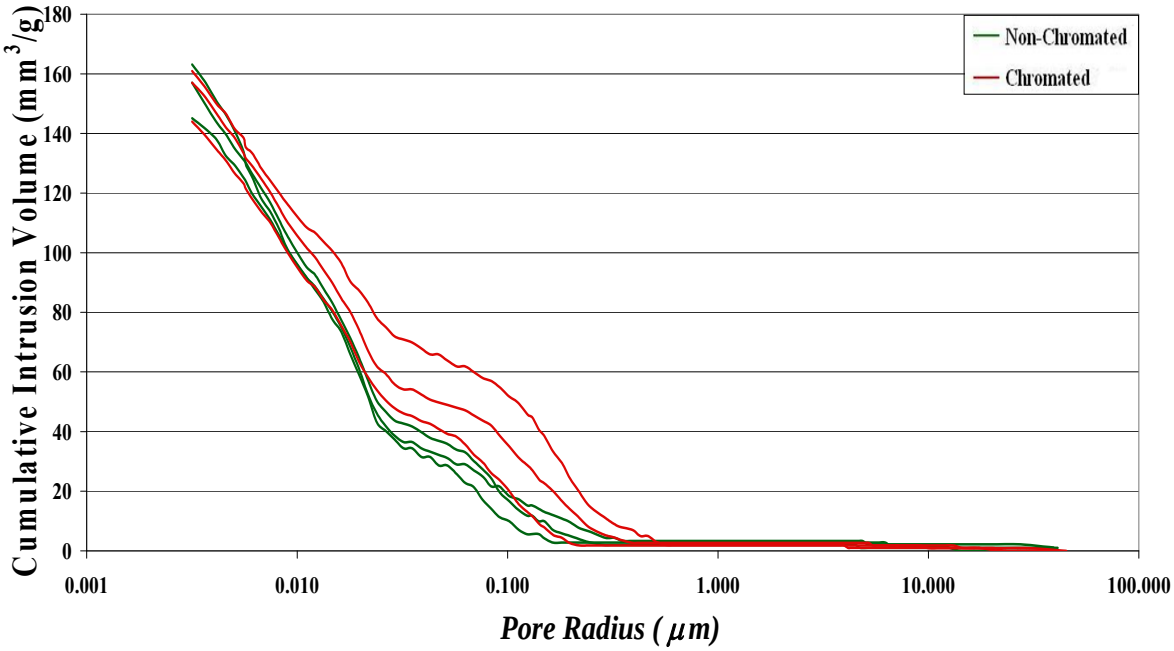

Figure 4-40. Pore size distribution of slag cement adjacent to HDG bars

A comparison of the total intruded volume for the different cement is provided by Table 4-3. The higher intrusion volume of the cement adjacent to uncoated bars, compared to those adjacent to HDG bars suggests that diffusion of the zinc corrosion products may be filling the cement pores. Regardless of the type of cement, there was insignificant difference in cumulative intrusion volume between the cement pastes adjacent to chromated and non-chromated bars. However, amongst the different cement types, both the silica fume and slag cement had the lower intrusion volumes than the OPC cement, which was expected as silica fume and slag are known to form additional C-S-H which reduces the pore space. This observation is in agreement with the resistance data presented above, where the higher resistance of both the silica fume and slag concrete compared to the OPC concrete indicates higher density and lower porosity.

Table 4-3. Summary of intrusion volumes

Sample		Total Intru. Vol. (mm^3/g)	Avg. Intru. Vol (mm^3/g)
OPC	Control 1	213	221
	Control 2	229	
	Control 3	237	
	Non-Chrom. 1	195	194
	Non-Chrom. 2	211	
	Non-Chrom. 3	176	
	Chrom. 1	227	206
	Chrom. 2	199	
	Chrom. 3	192	
Silica Fume	Non-Chrom. 1	132	134
	Non-Chrom. 2	135	
	Non-Chrom. 3	136	
	Chrom. 1	143	137
	Chrom. 2	134	
	Chrom. 3	134	
Slag	Non-Chrom. 1	157	155
	Non-Chrom. 2	145	
	Non-Chrom. 3	163	
	Chrom. 1	144	154
	Chrom. 2	161	
	Chrom. 3	157	

4.5 Microscopy of Hardened Cements

From EDS analysis, the depth at which zinc corrosion products diffuse into the adjacent cement was approximated. Figure 4-41 through Figure 4-46 are electron micrographs showing the zinc content of the cement from the bar/cement interface into the cement. The zinc content is

reported in weight percent of all the elements detected within the location of analysis. A zinc content of 1% or less is considered negligible since it falls within the error range of detection.

For OPC cements, the depths of diffusion are no more than 500μm and the type of bar does not seem to have an effect on this depth. In silica fume cement, the diffusion depth is considerably lower compared to OPC cement due to its lower porosity. The diffusion depth of the slag cement adjacent to non-chromated bar is comparable to the silica fume cements. The zinc contents near the bar/cement interface, however, are relatively lower. Since only one cement sample was examined, conclusive comments can not be made regarding this observation.

Regardless of the differences in diffusion depths and zinc contents observed for the different cements, the data confirmed that corrosion products did, in fact, diffuse into the cement, and therefore, also confirmed the hypothesis that the lower porosity for cement adjacent to HDG bars compared to cement adjacent to an uncoated steel bar, is in fact due to the diffusion of corrosion products, as discussed in the previous section.

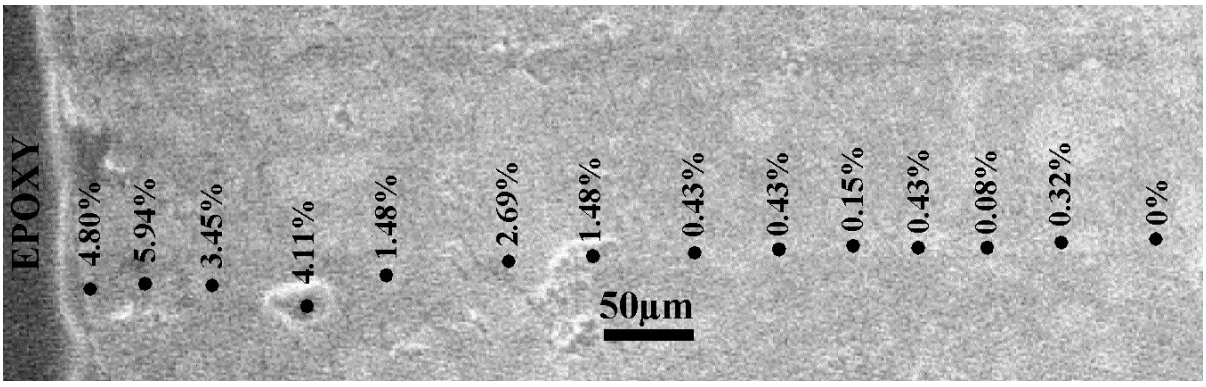

Figure 4-41. Zinc profile of OPC cement adjacent to a non-chromated bar

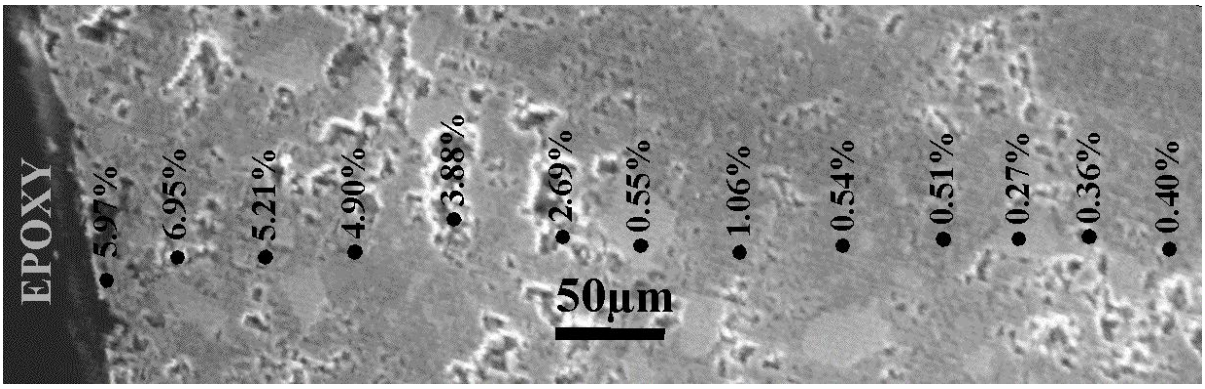

Figure 4-42. Zinc profile of OPC cement adjacent to a chromated bar

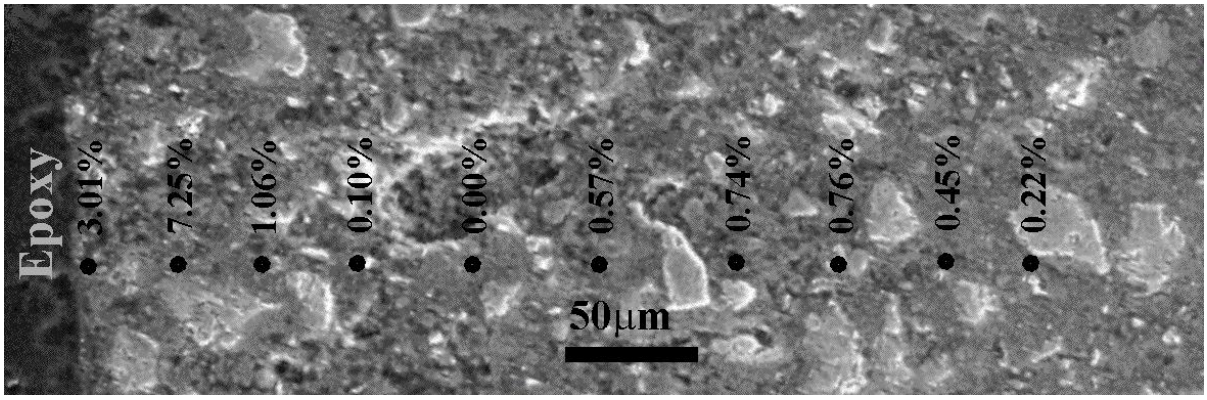

Figure 4-43. Zinc profile of silica fume cement adjacent to a non-chromated bar

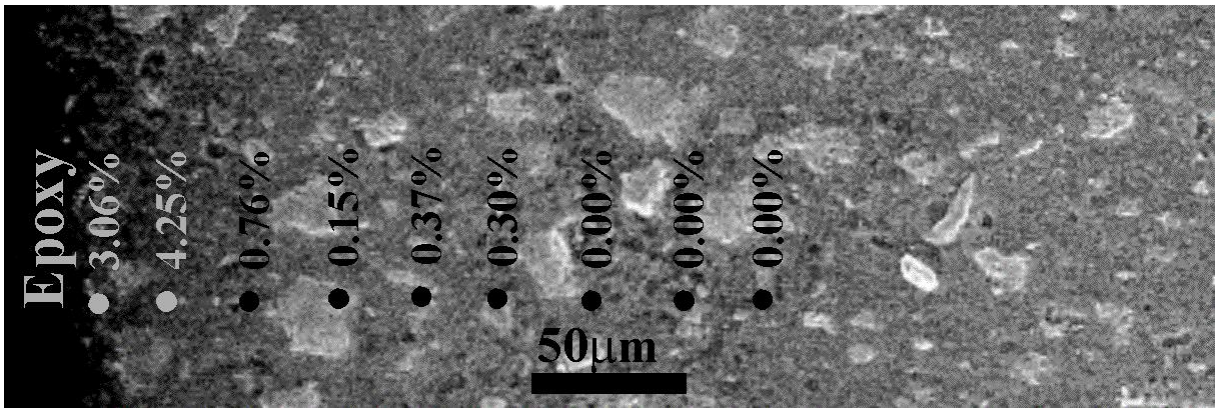

Figure 4-44. Zinc profile of silica fume cement adjacent to a chromated bar

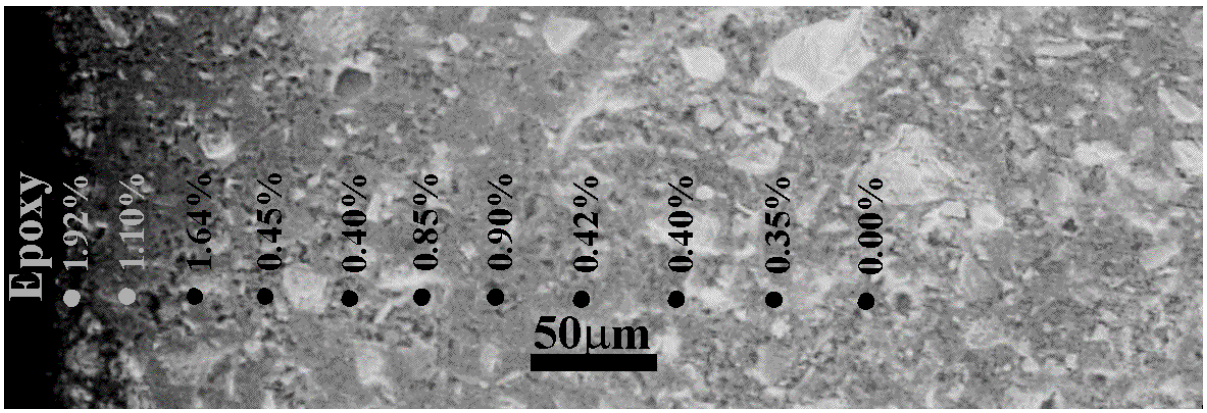

Figure 4-45. Zinc profile of slag cement adjacent to a non-chromated bar

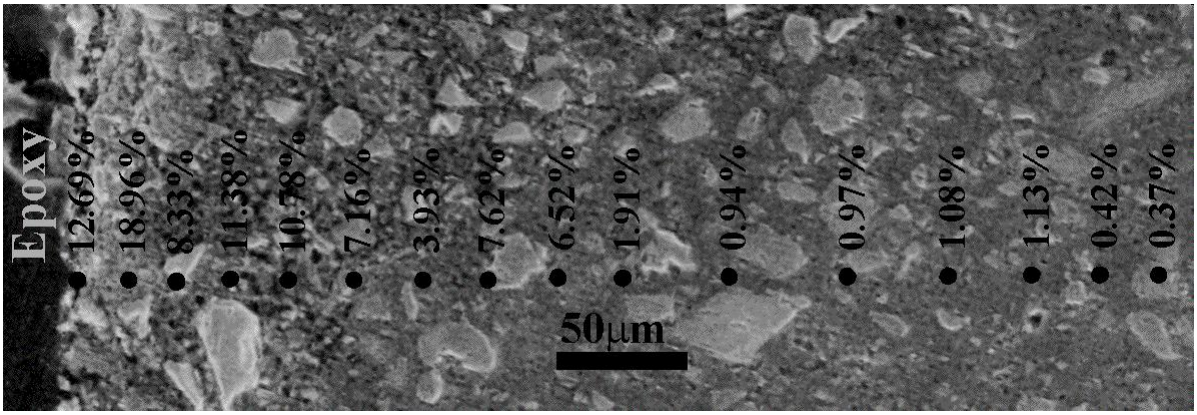

Figure 4-46. Zinc profile of slag cement adjacent to a chromated bar

Chapter 5
Summary and Conclusions

5.1 Effect of Coating Surface Composition on Corrosion

Based on the corrosion results in OPC concrete, annealing and weathering of galvanized coatings did not appear to have any significantly detrimental effects on their initial corrosion performance. Despite their deviations in corrosion behaviour compared to that of non-chromated bars, passivation was achieved.

In OPC concrete, chromate treatment did not improve the corrosion resistance of the galvanized coating. Instead, it retarded the formation of the CHZ layer which appeared to be more corrosion resistant than the chromate film itself. Therefore, when galvanized rebars are to be used in OPC concrete, chromate treatment is not recommended.

In OPC concrete, it appears that the non-chromated coating without any surface treatment provided the optimum corrosion protection because a higher amount of zinc is available at the eta surface layer, which allowed a passive layer of CHZ to form more rapidly.

5.2 Effect of Concrete Mixture on Corrosion

In the present study, cement replacement in the concrete by 8 wt% silica fume or 25 wt% by slag increased the initial corrosion of the HDG rebar significantly when compared to OPC concrete. This behaviour is attributed to a higher initial pH and its rate of increase of the pore solution in these concretes compared to that of OPC concrete.

In slag concrete, the initial corrosion rates for non-chromated bars were much higher than those in silica fume concrete. The cause of this behaviour is believed to be the slow reactivity of slag particles that, in turn, gave rise to higher water to binder ratio of the ordinary Portland cement component of the blended cement. Therefore, during the initial hours when the slag remained un-reacted, the hydrated cement was highly porous and allowed a higher ionic mobility, and hence, higher corrosion rates.

With a higher pH in the pore solution of the slag and silica fume concretes, passivation did not occur for either the chromated or the non-chromated bars. However, under these non-passivating

conditions, chromate treatment improved the initial corrosion resistance of the coatings. Over a period of time, however, non-chromated bars reached corrosion rates lower than those for chromated bars, due to formation of CHZ and hardening of the concrete. This observation further confirmed that chromate treatment is not necessary, even in the concretes containing silica fume and slag used in the present work.

In these concretes, if sufficient passivation was not achieved prior to approximately two days, a subsequent increase in the corrosion rate can occur due to reactivity of the silica fume and slag particles. As concrete continues to harden and more CHZ is formed, the corrosion rate gradually decreases and can be assumed to reach a passive state over time.

5.3 Coating Depth Loss

Since passivation was achieved for all type of bars in OPC concrete, the coating depth losses for all types of HDG bars were considered insignificant (less than 1.5 μm before passivation). However, due to high initial corrosion rates and lack of passivity in both the silica fume and slag concretes, losses on average, were much higher and are considered detrimental to the overall protection provided by the coatings.

5.4 Autopsy of Corroded Bars

Through Raman spectroscopy, CHZ was confirmed to be present on all bars. CHZ was responsible for the passive corrosion observed in OPC concretes. On chromated bars, the frequency of detecting CHZ was lower compared to non-chromated bars, which indicated that the chromate film retarded the formation of CHZ.

For bars exposed to silica fume and slag concretes, large amounts of zinc oxide and lower amounts of CHZ were detected due to higher pH measured in these concretes compared to that of OPC concrete.

5.5 Impact of Hydrogen Evolution on Adjacent Cement Porosity

Hydrogen evolution does not appear to increase the pore volume of cement adjacent to HDG bars. The difference in mercury intrusion volume between the OPC cements adjacent to the uncoated bars and the HDG bar was insignificant. Any additional pores produced by hydrogen evolution are

likely filled by corrosion products of zinc, which were found to penetrate approximately 500μm into the concrete adjacent to the steel.

Chromating did not show any detectable effect in reducing hydrogen evolution, as the differences in intrusion volumes between cements adjacent to chromated and non-chromated bars were negligible.

Silica fume and slag cements had significantly lower pore volumes compared to OPC cements, which is attributed to the formation of additional C-S-H.

Chapter 6
Recommendations

Based on the corrosion results for the silica fume and slag concrete specimens, addition of either silica fume or slag to concrete appeared to have major influences on the corrosion rate and the time required for passivation. Since the concrete mix designs used in Ontario, Canada often contain both silica fume and slag, the effect of this combination on the corrosion behaviour should be investigated.

As shown by the work of Larbi et al.[31], with higher pH in concrete containing silica fume, the calcium concentration decreased at a faster rate compared to ordinary Portland cement concrete. As the calcium in concrete pore fluid is required for the formation of calcium hydroxyzincate, quantification of its concentration in the different concretes used in the present work may provide additional insight in corrosion behaviour observed in the different concretes. Furthermore, quantification of other major anions and cations can confirm the pH measured in this study. Therefore, pore solution analysis at different ages is recommended.

Additional cement samples should be analysed through electron microscopy and energy dispersive x-ray spectroscopy to produce more representative results regarding the diffusion of zinc corrosion products. Furthermore, samples with varying degrees of hydration could be studied to determine diffusion depth as a function of hydration time.

For further work in this area, corrosion and pH monitoring should be carried out in a controlled environment to eliminate any effects of temperature and relative humidity fluctuation.

Bibliography

1. Slater, W.A., Richard, F.E., & Scofield, G.G., *Tests on bond resistance between concrete and steel, Technical Paper No. 173*, U.S. National Bureau of Standards. 1920. p. 9-33.
2. Robinson, K.E., *The bond strength of galvanized reinforcement*, in *Technical Report TRA/220*. 1956, Cement and Concrete Association: London. p. 7.
3. Kayali, O., & Yeomans, S.R., *Bond and slip of coated reinforcements in concrete.* Construction and Building Materials, 1995. **9**(4): p. 219-226.
4. Kayali, O., & Yeomans, S.R., *Bond of galvanized steel in concrete.* Cement and Concrete Composites, 2000. **22**(6): p. 459-467.
5. Blanco, M.T., Andrade, C., & Macias, A. , *SEM study of corrosion products of galvanized reinforcements immersed in solutions on the pH range 12.6 to 13.6.* British Corrosion Journal, 1984. **19**(1): p. 41-48.
6. Marder, A.R., *The metallurgy of zinc-coated steel.* Progress in Materials Science, 2000(45): p. 191-271.
7. Andrade, C., & Alonzo, C., *Electrochemical Aspects of Galvanized Steel*, in *Galvanized Steel Reinforcement in Concrete*, S.R. Yeomans, Editor. 2004, Elsevier. p. 111-143.
8. Langill, T.J., & Dugan, B., *Zinc Materials for Use in Concrete*, in *Galvanized Steel Reinforcement in Concrete*, S.R. Yeomans, Editor. 2004, Elsevier. p. 87-109.
9. *Galvanized Steel Reinforcement in Concrete* ed. S.R. Yeomans. 2004: Elsevier. 118.
10. Roetheli, B.E., Cox, G.L., & Littreal, W.B. , *Effect of pH on the corrosion products and corrosion rate of zinc in oxygenated aqueous solutions.* Metals and Alloys, 1932. **3**: p. 73-76.
11. Shams El Din, A.M., Adb El Wahab, F.M., & Abd El Haleem, S.M., *Effect of electrolyte concentration on the passivation of Zn in alkaline solutions.* Werkstoff and Korrosion, 1973. **24**: p. 389-394.
12. Liebau, F., & Amel-Zadeh, A. , *The crystal structure of $Ca(Zn_2(OH)_6 2H_2O$ - a retarder in the setting of Porland cement.* Kistall und Technik, 1972. **7**(1-3): p. 221-227.
13. Vorkapic, L.Z., Drazic, D. M., & Despic, A. R., *Corrosion of pure and amalgamated zinc in concentrated alkalki hydroxide solutions.* Journal of Electrochemical Society, 1974. **121**(11): p. 1385-1392.
14. Lieber, W., & Gebauer, J., *Einbau von zink in calcium silicathydrate.* Zement-kalk-Gips, 1970. **4**(161-164).
15. Macias, A., & Andrade, C., *Corrosion of galvanized steel reinforcement in alkaline solutions.* British Corrosion Journal, 1987. **22**(2): p. 133-138.
16. Macias, A., & Andrade, C. , *Stability of the calcium hydroxizincate protective layer developed on galvanized reinforcement after a further increase of the pH value.* . Materials de Construccion, 1986. **36**(204): p. 19-27.
17. Gonzàlez, J.A., Vargas, R., & Andrade, C., *Revisión sobre el comportamiento de las armaduras galvanizadas en el hormigón.* Hormigón y Acero, 1977. **124**(113-132).
18. *Galvanized Steel Reinforcement in Concrete* S.R. Yeomans, Editor. 2004, Elsevier. p. 118-119.
19. Kayali, O., *Bond of steel in concrete and the effect of galvanizing*, in *Galvanized Steel Reinforcement in Concrete*, S.R. Yeomans, Editor. 2004, Elsevier. p. 229-270.
20. Kayali, O., & Yeomans, S.R., *Bond of ribbed galvanized reinforcing steel in concrete.* Cement and Concrete Composites, 2000. **22**(6): p. 459-467.
21. Belaïd, F., Arliguie, G., & Fançois, R. , *Effect of bar properties on bond strength of galvanized reinforcement* Journal of Materials in Civil Engineering, 2001. **16**(6): p. 454-458.

22. Fratesi, R., Moriconi, G., & Coppola, L., *The influence of steel galvanisation on rebar behaviour in concrete*, in *Corrosion of reinforecment in concrete construction*, P.B.B. C. L. Page, & J. W. Figg, Editor. 1996, The Royal Society of Chemistry: UK. p. 631-641.
23. Magalhães, A.A.O., Margarit, I.C.P., & Mattos, O.R., *Electrochemical characterization of chromate coatings on galvanized steel.* Electrochimica Acta, 1999. **44**: p. 4281-4287.
24. Mekhalif, Z., Forget, L., & Delhalle, J., *Investigation of the protective action of chromate coatings on hot-dip galvanized steel: role of wetting agents.* Corrosion Science, 2005. **47**: p. 547-566.
25. Ivanova, V., Raichevsky, G., Vitkova, St., & Nikolova, M. , *Protective ability of chromate passive films on electrodeposited zinc-tin alloys.* Surface and Coating Technology, 1996. **82**: p. 232-238.
26. Forget, L., Delhalle, J., & Mekhalif, Z. , *Application of scanning Kelvin probe to study the corrosion protection of chromated hot-dip galvanized steel.* Materials and Corrosion, 2001. **52**: p. 181-184.
27. Short, N.R., Zhou, S., & Dennis, J. K. , *Electrochemical studies on the corrosion of a range of zinc alloy coated steel in alkaline solutions.* Surface and Coating Technology, 1996. **79**: p. 218-224.
28. Heydarzadeh Sohi, M., & Jalali, M., *Study of the corrosion properties of zinc-nickel alloy electrodeposits before and after chromating.* Journal of Materials Processing Technology, 2003(138): p. 63-66.
29. Singh, A.K., Jha, G., Rani, N., Bandyopadhyay, N., & Venugopalan, T., *Premature darkening problem and its prevention in galvanized sheet surface.* Surface and Coating Technology, 2006(200): p. 4897-4903.
30. Long, Z.L., Zhou, Y.C., & Xiao, L., *Characterization of black chromate conversion coating on the electrodeposited zinc-iron alloy.* Applied Surface Science, 2003. **218**: p. 123-136.
31. Larbi, J.A., Fraay, A.L.A., & Bijen, J.M.J.M. , *The chemistry of the pore fluid of silica fume-blended cement systems.* Cement and Concrete Composites, 1990. **20**: p. 506-516.
32. Hooton, R.D., *Canadian use of ground granulated blast-furnace slag as a supplementary cementing material for enhanced performance of concrete.* Canadian Journal of Civil Engineering, 2000. **27**: p. 754760.
33. Callister, W.D.J., *Materials Science and Engineering*. 5th ed.. 2000: John Wiley & Sons Inc. 53-57.
34. Stern, M., & Geary, A. L., *Electrochemical polarization: I. A theoretical analysis of the shape of polarization curves.* Journal of Electrochemical Society, 1957. **104**(1): p. 55-63.
35. Gonzàlez, J.A.A., C., *Effect of carbonation, chlorides and relative ambient humidity on the corrosion of galvanized rebars embedded in concrete.* British Corrosion Journal, 1982. **17**(1): p. 21-28.
36. Jones, D.A., *Electrochemical Kinetics of Corrosion*, in *Principles and Prevention of Corrosion*. 1996, Prentice Hall: Upper Saddle River, NJ. p. 75-97.
37. Du, R.G., Hu, R.G., Huang, G.S., & Lin, C.J. , *In situ measurement of Cl^- concentration and pH at the reinforcing steel/concrete interface by combination sensors.* Journal of Analytical Chemistry, 2006. **78**: p. 3179-3185.
38. Lin, T.C., Mollah, M.Y.A., Vempati, R.K., & Cocke, D.L. , *Synthesis and characterization of calcium hydroxyzincate using x-ray diffraction, FT-IR spectroscopy, and scanning force microscopy.* Chemistry of Materials, 1995. **7**: p. 1974-1978.
39. Min, D., & Mingshu, T. , *Formation and expansion of ettringite crystals.* Cement and Concrete Research, 1994. **24**(1): p. 119-126.